

## **Dynamic identification of $\hat{\pi}$ in $Y\pi = \tau$ and extraction of physical parameters $\hat{p}$ .**

Estimation of internal wrenches using Newton-Euler algorithms: effect of the presence or not of physical constraints on parameters.

Simionato Giada

1822614

# Contents

<b>Abstract</b>	<b>1</b>
<b>1 Introduction</b>	<b>1</b>
<b>2 Preliminaries</b>	<b>2</b>
2.1 Dynamic Model Computation . . . . .	3
2.1.1 Euler-Lagrange formulation . . . . .	3
2.1.2 Newton-Euler formulation . . . . .	4
2.2 Dynamic Coefficients Identification . . . . .	4
2.3 Dynamic Parameters Extraction . . . . .	5
2.4 Newton-Euler Algorithm . . . . .	7
<b>3 Robot Structures</b>	<b>9</b>
3.1 3R Spatial Manipulator . . . . .	9
3.2 KUKA LWR IV+ 7R Robot . . . . .	11
<b>4 Framework</b>	<b>14</b>
<b>5 Experimental Details and Results</b>	<b>17</b>
5.1 3R Spatial Manipulator . . . . .	17
5.2 3R Spatial Manipulator with Friction Model and Gaussian Noise . . . . .	23
5.3 KUKA LWR IV+ 7R . . . . .	25
5.4 KUKA LWR IV+ 7R with Friction Model and Gaussian Noise . . . . .	31
<b>6 Conclusions</b>	<b>35</b>
<b>A Supplementary Material</b>	<b>36</b>
<b>References</b>	<b>42</b>

## **Abstract**

In this work a complete procedure over different manipulators aimed at deriving their dynamic models was performed, identifying the corresponding dynamic coefficients and from these, extracting sets of parameters. Finally the behaviours of the internal wrenches were studied and compared from those being generated from *feasible*, *unfeasible* and ground-truth sets of parameters. This framework was applied to the *3R spatial anthropomorphic manipulator* and to the *7R KUKA LWR IV+*, both either with and without friction phenomena modelling. A deep analysis at the *reason-of-unfeasibility* level was performed.

# Chapter 1

## Introduction

In this work the aim of analysing the behaviour of the internal wrenches of several manipulators was addressed, with respect to having being generated from feasible and unfeasible sets. Two different robots with two versions for each were taken into consideration: the *3R spatial anthropomorphic* manipulator, the *7R KUKA LWR IV+* and both robots augmented with friction modelling. Dynamic models were derived while dynamic coefficients for each of these robots were identified. Then dynamic parameters sets were extracted and by the relaxation of bounds and loss functions, sets of parameters either feasible or unfeasible were obtained. Finally the internal forces behaviours were retrieved and studied.

The keypoints of this work are the fact that the entire procedure provided dynamic coefficients and parameters either for proof-of-concept models, such as the 3R, and for real ones, like the KUKA 7R, and the deeper analysis conducted over the comparisons of the behaviour of the internal wrenches. In this latter case the study was conducted not only at the level of *feasibility-unfeasibility* duality, but also the *reasons* behind the unfeasibility were investigated, trying to find a connection between the type of violation and the behaviour of the internal wrenches.

This work is based on the procedures and mathematical results described in papers [1, 2, 3, 4]. This report is organized as follows: in Chapter 2 preliminary theoretical notions are presented, focusing on the building of the dynamic model (Section 2.1), on the dynamic coefficients identification phase (Section 2.2), on the extraction procedure of dynamic parameters (Section 2.3) and on the use of the Newton-Euler algorithm for retrieving internal wrenches and how to handle them (Section 2.4). In Chapter 3 a description of the robots used in this work is reported along with their schemas, reference frames and *Denavit-Hartenberg* parameters. In Chapter 4 an explanation of the framework developed for this work will be presented while in Chapter 5 the results for the 3R (Section 5.1), for the 3R with friction (Section 5.2), for the 7R (Section 5.3) and for the 7R with friction (Section 5.4) will be provided, commented and analysed. Finally, in Chapter 6 conclusions will be drawn.

# Chapter 2

## Preliminaries

In a manipulator, each of the links from which it is made up, is characterized by 10 dynamic parameters: therefore, a robot with  $n$  links will be described by  $10n$  such parameters.

The first of these quantities is the *mass* of the link, denoted as  $m_i$  with  $i = 1, \dots, n$ , while other three parameters are the *coordinates of the center of mass* (CoM) of the link along the three directions of its reference frame. These values can be collected in the vector:

$${}^i \mathbf{r}_{i,ci} = \begin{pmatrix} c_{ix} \\ c_{iy} \\ c_{iz} \end{pmatrix} \quad \text{with } i = 1, \dots, n. \quad (2.1)$$

The last six parameters are the *elements of the inertia tensor* of the link<sup>1</sup> denoted as in Eq. (2.2) with respect to the  $i$ -th link frame.

$${}^i \mathbf{J}_{l_i} = \begin{pmatrix} J_{ixx} & J_{ixy} & J_{ixz} \\ J_{ixy} & J_{iyy} & J_{iyz} \\ J_{ixz} & J_{iyz} & J_{izz} \end{pmatrix} \quad \text{with } i = 1, \dots, n. \quad (2.2)$$

Summarizing, these parameters, ten for each link, can be collected in three vectors:

$$\begin{aligned} \mathbf{p}_1 &= (m_1 \ \dots \ m_n)^T \\ \mathbf{p}_2 &= (c_{1x}m_1 \ c_{1y}m_1 \ c_{1z}m_1 \ \dots \ c_{nx}m_n \ c_{ny}m_n \ c_{nz}m_n)^T \\ \mathbf{p}_3 &= (\mathcal{J}_1^T \ \dots \ \mathcal{J}_n^T)^T \end{aligned} \quad (2.3)$$

with  $\mathbf{p}_1 \in \mathbb{R}^n$ ,  $\mathbf{p}_2 \in \mathbb{R}^{3n}$ ,  $\mathbf{p}_3 \in \mathbb{R}^{6n}$  and

$$\mathcal{J}_i = (J_{ixx} \ J_{ixy} \ J_{ixz} \ J_{iyy} \ J_{iyz} \ J_{izz}) \quad \text{with } i = 1, \dots, n. \quad (2.4)$$

Finally, these components are organized into a common vector  $\boldsymbol{\pi} \in \mathbb{R}^{10n}$  of dynamic parameters, as in Eq. (2.5):

$$\boldsymbol{\pi}(\mathbf{p}_1, \mathbf{p}_2, \mathbf{p}_3) = (\mathbf{p}_1^T \ \mathbf{p}_2^T \ \mathbf{p}_3^T)^T. \quad (2.5)$$

In the case in which also the friction effect is modelled, the dynamic parameters for each link become 13, i.e.  $13n$  for a  $n$ -dofs manipulator. These additional values,  $f_{v,i}$ ,  $f_{c,i}$  and  $f_{o,i}$ , represent the *viscous friction*, the *Coulomb friction* and the *Coulomb friction offset* respectively. By collecting these parameters for each link, it's possible to augment the vectors in Eq. (2.3) with those in Eq. (2.6):

---

<sup>1</sup>Even if the inertia tensor is a  $3 \times 3$  matrix, due to its symmetry, only six elements are distinguishable and therefore can be counted as dynamic parameters.

$$\begin{aligned}\mathbf{p}_4 &= (f_{c1} \ \cdots \ f_{cn})^T \\ \mathbf{p}_5 &= (f_{v1} \ \cdots \ f_{vn})^T \\ \mathbf{p}_6 &= (f_{o1} \ \cdots \ f_{on})^T,\end{aligned}\tag{2.6}$$

and therefore Eq. (2.5) becomes:

$$\boldsymbol{\pi}(\mathbf{p}_1, \mathbf{p}_2, \mathbf{p}_3, \mathbf{p}_4, \mathbf{p}_5, \mathbf{p}_6) = (\mathbf{p}_1^T \ \mathbf{p}_2^T \ \mathbf{p}_3^T \ \mathbf{p}_4^T \ \mathbf{p}_5^T \ \mathbf{p}_6^T)^T \in \mathbb{R}^{13n}.\tag{2.7}$$

In order to analyse the behaviour of these parameters it is first necessary to derive the dynamic model of the manipulator, as described in the next section.

## 2.1 Dynamic Model Computation

For deriving the dynamic model of a manipulator it's possible to use two different algorithms that produce the same formulation: the *Euler-Lagrange* and the *Newton-Euler* procedures. In this work both these algorithms were developed and used, but the latter, due to its recursive nature and the lack of instructions such as `collect(...)` or `simplify(...)` in favour of a more tensor-based approach, it was found to be incredibly faster<sup>2</sup> than the former. Here a brief theoretical dissertation, based on [4], on the two approaches will be presented.

### 2.1.1 Euler-Lagrange formulation

Being  $\mathbf{q} \in \mathbb{R}^n$  the set of the generalized coordinates, the total kinetic energy, using the *König* theorem for each link, is:

$$\mathcal{T} = \sum_{i=1}^n \mathcal{T}_{l_i} = \frac{1}{2} \sum_{i=1}^n (m_i^i \mathbf{v}_{ci}^{Ti} \mathbf{v}_{ci} + {}^i \mathbf{w}_i^{Ti} \mathbf{I}_{l_i} {}^i \mathbf{w}_i),\tag{2.8}$$

with the meaning of the symbols as in [4]. The total potential energy is given by Eq. (2.9):

$$\mathcal{U} = \sum_{i=1}^n \mathcal{U}_{l_i} = - \sum_{i=1}^n m_i \boldsymbol{\gamma}^T \mathbf{r}_{0,ci},\tag{2.9}$$

while the inertia matrix  $\mathbf{M}(\mathbf{q})$  and the gravity vector  $\mathbf{g}(\mathbf{q})$  are derived as in Eq. (2.10) and Eq. (2.11).

$$\mathbf{M}(\mathbf{q}) = \nabla_{\dot{\mathbf{q}}}^2 \mathcal{T}(\mathbf{q}, \dot{\mathbf{q}}),\tag{2.10}$$

$$\mathbf{g}(\mathbf{q}) = \nabla_{\mathbf{q}} \mathcal{U}(\mathbf{q}).\tag{2.11}$$

The Coriolis and centrifugal term  $\mathbf{S}(\mathbf{q}, \dot{\mathbf{q}})\dot{\mathbf{q}}$  is obtained by analytical differentiation of the elements of the inertia tensor.

---

<sup>2</sup>In the 7R manipulator the Euler-Lagrange routine took more than 50 hours of continuous computations, versus the seven minutes of the Newton-Euler one. More details on this will be disclosed in Section 5.3

### 2.1.2 Newton-Euler formulation

This recursive algorithm is developed in three phases based on the Newton and Euler's equations. The notation used here is the conventional one for the dynamic elements<sup>3</sup>.

The first phase is the *forward* step and for each link from the base towards the end-effector, these equations are computed:

$$\begin{aligned} {}^i w_i &= {}^{i-1} R_i^T [{}^{i-1} w_{i-1} + \dot{q}_i {}^{i-1} z_{i-1}] \quad \text{init : } w_0 = 0; \\ {}^i \dot{w}_i &= {}^{i-1} R_i^T [{}^{i-1} \dot{w}_{i-1} + \ddot{q}_i {}^{i-1} z_{i-1} + \dot{q}_i {}^{i-1} w_{i-1} \times {}^{i-1} z_{i-1}] \quad \text{init : } \dot{w}_0 = 0; \\ {}^i a_i &= {}^{i-1} R_i^T {}^{i-1} a_{i-1} + {}^i \dot{w}_i \times {}^i r_{i-1,i} + {}^i w_i \times ({}^i w_i \times {}^i r_{i-1,i}) \quad \text{init : } a_0 - {}^0 g = 0; \\ {}^i a_{ci} &= {}^i a_i + {}^i \dot{w}_i \times {}^i r_{ci,i} + {}^i w_i \times ({}^i w_i \times {}^i r_{ci,i}). \end{aligned} \quad (2.12)$$

The backward step instead computes the forces and the torques acting on the link in a backward fashion using Eq. (2.13):

$$\begin{aligned} f_i &= f_{i+1} + m_i(a_{ci}) \quad (\text{gravity inside forward step}); \\ \tau_i &= \tau_{i+1} + f_i \times (r_{i-1,i} + r_{i,ci}) + f_{i+1} \times r_{i,ci} + I_i \dot{w}_i + w_i \times (I_i w_i). \end{aligned} \quad (2.13)$$

The final step consists on the projection of the wrenches along the *z-axis* through Eq. (2.14) to obtain the generalized forces in the right-hand side of the well-known Euler-Lagrange equation.

$$u_i = \begin{cases} f_i^{Ti} z_{i-1} + \eta_i \dot{q}_i & \text{for prismatic joint} \\ \tau_i^{Ti} z_{i-1} + \eta_i \dot{q}_i & \text{for revolute joint} \end{cases} \quad (2.14)$$

However, both the approaches provide the formulation of the motor torques in Eq. (2.15):

$$\mathbf{M}(\mathbf{q}) \ddot{\mathbf{q}} + \mathbf{S}(\mathbf{q}, \dot{\mathbf{q}}) \dot{\mathbf{q}} + \mathbf{g}(\mathbf{q}) = \boldsymbol{\tau}. \quad (2.15)$$

In order to add the friction model to Eq. (2.15), it's possible to add the linear term in Eq. (2.16) to Eq. (2.15) obtaining Eq. (2.17).

$$\tau_{f,j}(\dot{q}_j) = f_{v,j} \dot{q}_j + f_{c,j} \text{sign}(\dot{q}_j) + f_{o,j}. \quad (2.16)$$

The coefficients in Eq. (2.16) have the same meaning explained in Chapter 2.

$$\mathbf{M}(\mathbf{q}) \ddot{\mathbf{q}} + \mathbf{S}(\mathbf{q}, \dot{\mathbf{q}}) \dot{\mathbf{q}} + \mathbf{g}(\mathbf{q}) + \boldsymbol{\tau}_f = \boldsymbol{\tau}. \quad (2.17)$$

## 2.2 Dynamic Coefficients Identification

Looking at the Eq. (2.15) or (2.17) of the dynamic model of a manipulator, without and with friction modelling respectively, is possible to notice that could be rearranged in such a way that the vector of dynamic parameters  $\boldsymbol{\pi}$  appears linearly, as in:

$$\mathbf{Y}(\mathbf{q}, \dot{\mathbf{q}}, \ddot{\mathbf{q}}) \boldsymbol{\pi} = \boldsymbol{\tau} \quad (2.18)$$

where  $\mathbf{Y}$  ( $\in \mathbb{R}^{n \times 10n}$  or  $\in \mathbb{R}^{n \times 13n}$  in presence of friction) is the *regressor matrix*. Since the dynamic parameters now appear linearly in the dynamic model equations, the regressor matrix could be obtained as the symbolic Jacobian of those equations with respect to the vector of dynamic parameters and depends only on the values of the joint positions, velocities and accelerations.

---

<sup>3</sup>Since all the elements are vectors or matrices a non-bold notation was adopted here for the ease of reading.

Even if the structure of Eq. (2.18) could suggest a least square approach to obtain  $\boldsymbol{\pi}$ , the internal behaviour of the regressor matrix doesn't allow to follow this procedure since it's not full column rank. This phenomena is due to the fact that not all the parameters play a role in the dynamic behaviour, or moreover some of them appear only in groups. These latter are known as *dynamic coefficients*, (or *base parameters*)[1] and for identifying them several exciting trajectories must be generated and sampled to obtain  $M$  samples under the *weak condition* of  $M \gg 10n$ .<sup>4</sup> Substituting each of the obtained samples  $(\tau_k, q_k, \dot{q}_k, \ddot{q}_k)$  in Eq. (2.18) and stacking them end up in Eq. (2.19),

$$\bar{\mathbf{Y}}\boldsymbol{\pi} = \bar{\boldsymbol{\tau}} \quad (2.19)$$

where  $\bar{\boldsymbol{\tau}} \in \mathbb{R}^{Mn}$  and  $\bar{\mathbf{Y}} \in \mathbb{R}^{Mn \times p}$  (with  $p = 10$  without friction and  $p = 13$  otherwise). Then it's possible to obtain the stacked regressor with full column rank, i.e.  $\bar{\mathbf{Y}}_R$ , and through a least-squares solution having:

$$\hat{\boldsymbol{\pi}}_R = \bar{\mathbf{Y}}_R^\# \bar{\boldsymbol{\tau}}. \quad (2.20)$$

with  $\hat{\boldsymbol{\pi}}_R \in \mathbb{R}^\rho$  vector of the above mentioned dynamic coefficients.

The last step in the identification procedure constitutes in the validation of the candidate dynamic coefficients obtained from the OLS problem. Through the non-stacked reduced regressor  $\mathbf{Y}_R$ , a sequence of torque values were obtained, as in Eq. (2.21), using a brand new trajectory to check whether the identified coefficients would mirror the behaviour of the original dynamics equations of Eq. (2.15) and Eq. (2.17).

$$\hat{\boldsymbol{\tau}} = \mathbf{Y}_R(\mathbf{q}, \dot{\mathbf{q}}, \ddot{\mathbf{q}})\hat{\boldsymbol{\pi}}_R. \quad (2.21)$$

## 2.3 Dynamic Parameters Extraction

For the reasons explained in the previous section, the  $\rho$  dynamic coefficients are regrouping of the  $p$  dynamic parameters and since  $\rho < p$ , the mapping that links those quantities is not bijective, therefore there are infinite sets of dynamic parameters that can be combined to form the set of dynamic coefficients. In addition, not all the parameters appear in the coefficients, therefore to obtain a complete set as solution it's necessary to use a *global optimization algorithm* (e.g. *simulated annealing* or *genetic algorithms*).

Even if a particular set of parameters is a solution of the optimization algorithm (that mainly tries to address the increasing similarity between the identified dynamic coefficients and those reconstructed by the extracted set of parameters at each iteration), it's possible to distinguish between two categories: *feasible* and *unfeasible*. Dynamic parameters are linked to physical quantities, hence they are prone to undergo physical meanings: therefore it's possible to establish constraints to describe their feasibility. The most relevant are:

- *Constraints on masses*: the mass of each link must be positive, i.e.

$$m_i > 0 \quad \text{for } i = 1, \dots, n. \quad (2.22)$$

- *Constraints on inertial elements*: the inertia tensor of link  $l_i$  with respect to its center of mass must be positive definite, i.e.

---

<sup>4</sup>In presence of friction the condition becomes  $M \gg 13n$ .

$$\mathbf{I}_{l_i} = \begin{pmatrix} I_{ixx} & I_{ixy} & I_{ixz} \\ I_{ixy} & I_{iyy} & I_{iyz} \\ I_{ixz} & I_{iyz} & I_{izz} \end{pmatrix} \succ 0, \quad \text{for } i = 1, \dots, n. \quad (2.23)$$

By exploiting its properties as highlighted in [1] and [3], it is possible to rewrite the constraint in Eq. (2.23) as Eq. (2.24):

$$\bar{I}_{i,x} > 0, \quad \bar{I}_{i,y} > 0, \quad \bar{I}_{i,z} > 0 \quad (2.24)$$

where these are the elements of the diagonal form of  $\mathbf{I}_{l_i}$  and therefore the eigenvalues of the original barycentric inertia matrix. Coping this observation with the additional constraint that must affect any inertia tensor, hence the *triangular inequality* [3] in Eq. (2.25), the final formulation of the constraint is obtained and reported in Eq. (2.26).

$$\begin{cases} \bar{I}_{i,x} + \bar{I}_{i,y} > \bar{I}_{i,z} \\ \bar{I}_{i,y} + \bar{I}_{i,z} > \bar{I}_{i,x} \\ \bar{I}_{i,z} + \bar{I}_{i,x} > \bar{I}_{i,y} \end{cases}, \quad (2.25)$$

$$\frac{\text{tr}(\mathbf{I}_{l_i})}{2} - \lambda_{\max}(\mathbf{I}_{l_i}) > 0. \quad (2.26)$$

- *Constraints on centers of mass:* depending on the shape of the links of the robot under consideration, it is possible to assess constraints on the coordinates of the CoMs. If the links have known *non-convex* geometrical shape, limits can be devised from a geometric parametrization of the boundaries of the link shape in all the three directions. For the sake of clarity, in the case of parallelepiped-shaped links, the box constraints are in the form of Eq. (2.27).

$$\begin{cases} c_{ix_{\min}} \leq c_{ix} \leq c_{ix_{\max}} \\ c_{iy_{\min}} \leq c_{iy} \leq c_{iy_{\max}} \\ c_{iz_{\min}} \leq c_{iz} \leq c_{iz_{\max}} \end{cases} \quad \text{for } i = 1, \dots, n \quad (2.27)$$

where the boundaries depends either on the geometric shape of the link and the knowledge of its density distribution.

Summarizing, in order to be feasible, a set of dynamic parameters must satisfy constraints in Eq. (2.22), (2.26) and, for example, (2.27), for all the links of the manipulator.

The global optimization algorithm used in this work is based on the Algorithm 1.

---

**Algorithm 1:** Parameters retrieval algorithm

---

**Result:** Set of dynamic parameters

$\mathbf{p}_0 \leftarrow LB + (UB - LB)\mathbf{u};$

$\xi_i \leftarrow 0;$

**for**  $k=1, \dots, \kappa$  **do**

$p_{k,\text{init}} \leftarrow p_{k-1};$

Solve  $\min_{\mathbf{p}_k} f(\mathbf{p}_k) = \phi(\mathbf{p}_k) + \xi_k \gamma(\mathbf{p}_k)$  s.t.  $LB \leq \mathbf{p}_k \leq UB$  ;

$\xi_{k+1} \leftarrow 10k;$

**end**

---

This algorithm is based on the use of *upper* and *lower* bounds, i.e. UB and LB respectively, for each parameter. These values can be identified thanks the geometry of the links or the knowledge gathered from the datasheet of the manipulator. Initially the set of dynamic

parameters are drawn according to the uniform random variable  $\mathbf{u} \sim \mathcal{U}(0, 1)$  between LB and UB and then updated according to the recursive solution of the GOA<sup>5</sup>.  $\xi_i$  is an increasing *penalty coefficient* that grows by ten times at each iteration and it's used to weight the violation of the external constraints. For each run the solution step of the global optimization algorithm is repeated several times and consists of solving a minimization problem of a cost function subject to the belonging of the parameters to the bounds intervals. The loss function is composed by an *internal* and an *external* term. The former is the squared Euclidean distance between the identified coefficients and those reconstructed from the extracted set of parameters, as shown in Eq. (2.28). Alternatively to this *two-steps* approach, it is possible to use a more precise *one-step* procedure, such as in Eq. (2.29). In this work only the first expression of  $\phi$  was used due to the fact that the second one involves the whole stacked regressor at each iteration, hence it required a enormous computational power.

$$\phi(\mathbf{p}_k) = \|\boldsymbol{\pi}(\mathbf{p}_k) - \hat{\boldsymbol{\pi}}\|^2 \quad (2.28)$$

$$\phi(\mathbf{p}_k) = \|\bar{\mathbf{Y}}\boldsymbol{\pi}(\mathbf{p}_k) - \bar{\boldsymbol{\tau}}\|^2 \quad (2.29)$$

The external loss value is the sum of  $\iota$  quantities, i.e.  $g_\iota(\cdot)$ , that represents the degree of violation of  $\iota$  constraints in the form of Eq. (2.22), (2.26) and (2.27), as reported in Eq. (2.30).

$$\gamma(\mathbf{p}_k) = \sum_{\iota} g(h_{\iota}(\mathbf{p}_k)) \quad (2.30)$$

In addition to the constrains on each mass, this latter term includes also a rule over the total mass of the manipulator that must me fall inside an interval of values collected from the datasheet, as shown in Eq. (2.31).

$$m_{tot,min} \leq \sum_i^n m_i \leq m_{tot,max} \quad (2.31)$$

Since this kind of algorithms are very sensitive to the solution landscape, to avoid to be stacked on local minima, it was exploit its randomness and the whole algorithm was repeated for  $\kappa$  runs, finally retaining only the best set of parameters based on the lowest loss value.

Finally the sets of extracted parameters can be validated using a similar approach to the one described in Section 2.2, through a new trajectory.

## 2.4 Newton-Euler Algorithm

The last step in this work was to analyse the behaviour of the *internal wrenches* of the manipulator using sets of *feasible* and *unfeasible* parameters extracted with the Algorithm 1. With a modification of the Newton-Euler routine used to compute the dynamic model of the manipulator as in Section 2.1, it's possible to retrieve also the internal wrenches acting on the joints in the form:

$$\mathbf{w} = \begin{pmatrix} f_{11} & f_{12} & \cdots & f_{1n} \\ f_{21} & f_{22} & \cdots & f_{2n} \\ f_{31} & f_{32} & \cdots & f_{3n} \\ m_{11} & m_{12} & \cdots & m_{1n} \\ m_{21} & m_{22} & \cdots & m_{2n} \\ m_{31} & m_{32} & \cdots & m_{3n} \end{pmatrix} \in \mathbb{R}^{6 \times n} \quad (2.32)$$

---

<sup>5</sup>Global Optimization Algorithm, e.g. simulated annealing.

The first three rows components of this matrix are the internal forces acting on the joints while the last three are their momenta. The next step is substituting in the symbolic version of Eq. (2.32) the values of the real, feasible or unfeasible sets of parameters combined with the values of the joint positions, velocities and accelerations according to a specific trajectory. Finally it's possible to plot the behaviour of the internal forces by computing the norm of the 3D vector for each joint, allowing a comparison.

# Chapter 3

## Robot Structures

In this work two different manipulators were taken as case study: the *3R spatial anthropomorphic* and the *KUKA LWR IV+ 7R*. In both cases the entire procedure **modelling-identification-extraction-plotting** was performed not only on the vanilla versions of those robots but also adding the friction model and a white Gaussian noise during the coefficients identification phase for more realistic estimation. In the following sections both the manipulators will be described in their features and kinematic parameters.

### 3.1 3R Spatial Manipulator

For academic purposes the first robot taken into consideration was a 3R spatial anthropomorphic manipulator, hence an open chain with three cylindrical links connected by means of revolute joints moving in a three-dimensional workspace. In order to develop the code for retrieving the dynamic model and to analyse its behaviour, were manually computed the reference frames attached to each joint using the classical *Denavit-Hartenberg* convention. The schema of the robot is depicted in Fig. 3.1(a) while in (b) its DH parameters are collected.

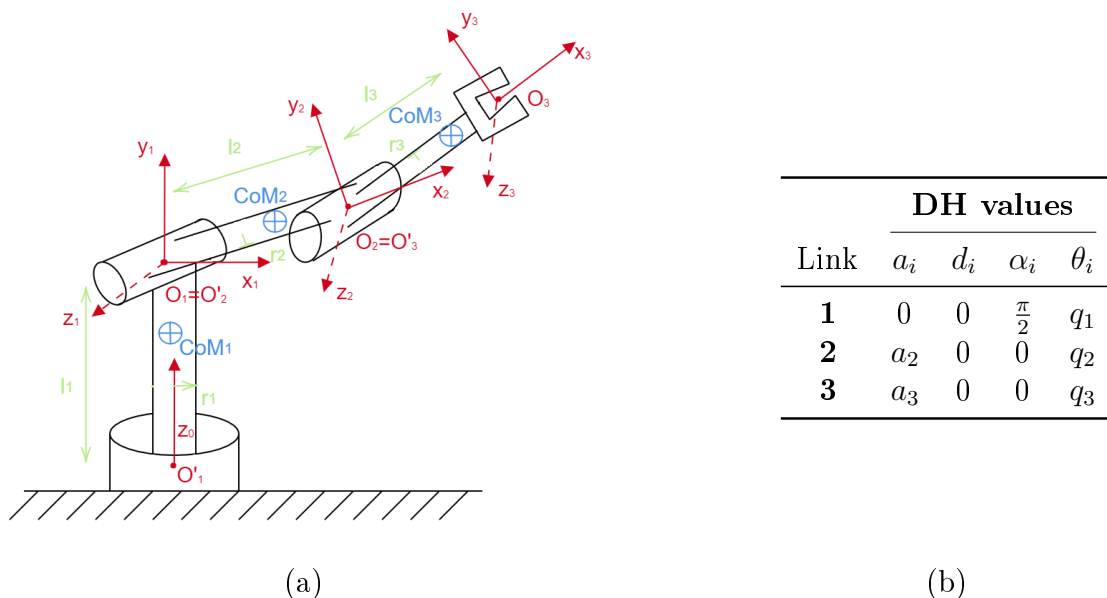


**Figure 3.1.** (a) 3R spatial manipulator scheme with DH reference frames; (b) DH parameters of the 3R spatial anthropomorphic manipulator.

Since in this work it was not possible to have a real version of the manipulator for collecting

the needed data such as torques and wrenches nor to compare obtained sets of dynamic parameters against a ground truth, particular values of the parameters were chosen as to simulate its behaviour. Starting from geometric values the others were manually derived either by choosing quantities as to provide challenging situations<sup>1</sup> or through physics formulae, i.e. *Steiner* theorem. The chosen values are integrally reported in Table 3.1 while geometric and kinematic ones in Table 3.2.

Parameter	Value	Parameter	Value	Parameter	Value
$m_1$	3.5 [kg]	$J_{1xy}$	3.15e-04 [Nm]	$J_{3xz}$	3.78e-04 [Nm]
$m_2$	0.8 [kg]	$J_{1xz}$	-1.4e-05 [Nm]	$J_{3yy}$	9.02e-03 [Nm]
$m_3$	1.2 [kg]	$J_{1yy}$	2.63e-02 [Nm]	$J_{3yz}$	-1.44e-05 [Nm]
$c_{1x}$	1e-03 [m]	$J_{1yz}$	6.3e-04 [Nm]	$J_{3zz}$	9.01e-03 [Nm]
$c_{1y}$	-12e-02 [m]	$J_{1zz}$	7.98e-02 [Nm]	$f_{v1}$	0.0665
$c_{1z}$	2e-03 [m]	$J_{2xx}$	4.98e-04 [Nm]	$f_{v2}$	0.1987
$c_{2x}$	-88e-03 [m]	$J_{2xy}$	1.27e-04 [Nm]	$f_{v3}$	0.0399
$c_{2y}$	1e-03 [m]	$J_{2xz}$	2.54e-04 [Nm]	$f_{c1}$	0.2450
$c_{2z}$	2e-03 [m]	$J_{2yy}$	1.34e-02 [Nm]	$f_{c2}$	0.1523
$c_{3x}$	-6e-02 [m]	$J_{2yz}$	-3.2e-06 [Nm]	$f_{c3}$	0.1827
$c_{3y}$	2e-03 [m]	$J_{2zz}$	1.34e-02 [Nm]	$f_{o1}$	-0.1073
$c_{3z}$	3e-03 [m]	$J_{3xx}$	5.71e-04 [Nm]	$f_{o2}$	-0.1566
$J_{1xx}$	5.64e-02 [Nm]	$J_{3xy}$	2.52e-04 [Nm]	$f_{o3}$	-0.0686

**Table 3.1.** Dynamic parameters values of the 3R spatial manipulator.

Quantity	Value
$l_1$	0.3 m
$l_2$	0.22 m
$l_3$	0.15 m
$r_1$	0.04 m
$r_2$	0.035 m
$r_3$	0.03 m
$a_2$	0.22 m
$a_3$	0.15 m

**Table 3.2.** Geometric and kinematic values of the 3R spatial manipulator.

Finally to make the simulations and the whole process as closer as possible to the reality, maximum and minimum bounds were imposed on the joint positions, velocities and accelerations. In order to have reliable values of those bounds, were used the ones of the first three links of the *Franka Emika Panda Robot*[1] and collected in Table 3.3.

<sup>1</sup>For example, the CoMs weren't lying in the cylinders' axes.

	Joint		
	1	2	3
<b>position</b>	2.8973	1.7628	2.8973
<b>velocity</b>	2.1750	2.1750	2.1750
<b>acceleration</b>	15	7.5	10

**Table 3.3.** Maximum values for the position, velocity and acceleration for each joint of the 3R spatial manipulator. Values are in [rad], [rad/s] and [rad/s<sup>2</sup>] respectively. Lower bounds are symmetric.

## 3.2 KUKA LWR IV+ 7R Robot

The entire framework was also applied on a real 7R manipulator: the *KUKA Large-Workspace-Robot (LWR) IV+*. This robot possesses seven revolute joints and thanks to the arbitrary choices in the classical DH convention applied to it, the only kinematic quantities are  $d_1$  and  $d_2$ . In Fig. 3.2(a) is shown the schema of the manipulator while in (b) its DH parameters are collected.

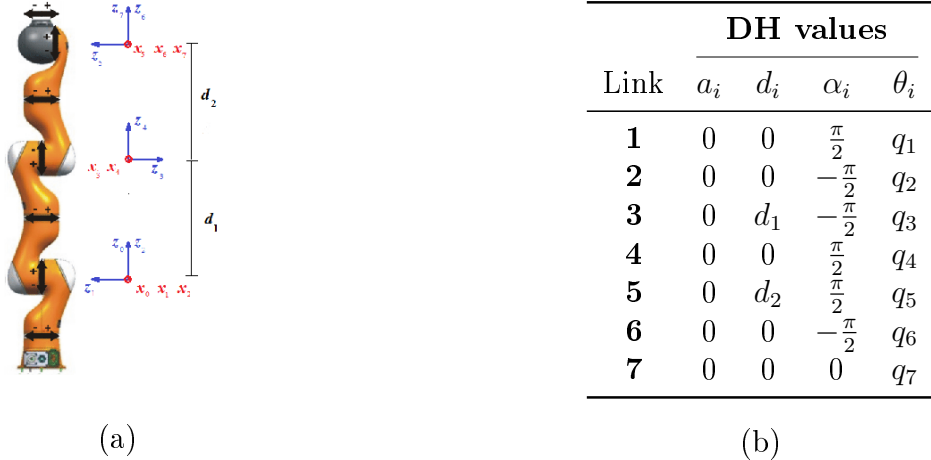


**Figure 3.2.** (a) KUKA LWR IV+ manipulator scheme in its zero position with DH reference frames; (b) corresponding DH parameters.

Even if the real manipulator owns the *Fast Research Interface Library* (FRI) from which it's possible to retrieve several useful information on the robot's state<sup>2</sup>, the tangible unavailability of the manipulator, made necessary to identify a ground-truth set of dynamic parameters in order to simulate its behaviour. For the sake of precision, it was chosen to use the closest values of its true dynamic parameters known in literature, namely those estimated in [2] e reported integrally in Table 3.4 together with its kinematic quantities.

<sup>2</sup>For example the link position  $q$ , the joint torque  $\tau_J$ , the numerical values of the link inertia matrix and the gravity vector with respect to the current robot's configuration.

Parameter	Value	Parameter	Value	Parameter	Value
$m_1$	2.7	$J_{1yy}$	6.887e-3	$J_{6yz}$	-7.008e-5
$m_2$	2.7	$J_{1yz}$	-2.681e-3	$J_{6zz}$	3.47e-3
$m_3$	2.7	$J_{1zz}$	0.03698	$J_{7xx}$	3-47e-3
$m_4$	2.7	$J_{2xx}$	0.039	$J_{7xy}$	0
$m_5$	1.7	$J_{2xy}$	9.415e-5	$J_{7xz}$	0
$m_6$	1.6	$J_{2xz}$	-3.145e-4	$J_{7yy}$	1.292e-3
$m_7$	0.3	$J_{2yy}$	0.03698	$J_{7yz}$	0
$c_{1x}$	1.34e-3	$J_{2yz}$	9.747e-3	$J_{7zz}$	1.584e-4
$c_{1y}$	-87.77e-3	$J_{2zz}$	6.887e-3	$f_{v1}$	0.0665
$c_{1z}$	-26.22e-3	$J_{3xx}$	6.887e-3	$f_{v2}$	0.1987
$c_{2x}$	1.34e-3	$J_{3xy}$	3.145e-4	$f_{v3}$	0.0399
$c_{2y}$	-26.22e-3	$J_{3xz}$	-9.5572e-5	$f_{v4}$	0.2257
$c_{2z}$	87.77e-3	$J_{3yy}$	6.8872e-3	$f_{v5}$	0.1023
$c_{3x}$	-1.34e-3	$J_{3yz}$	2.681e-3	$f_{v6}$	-0.0132
$c_{3y}$	87.77e-3	$J_{3zz}$	0.037	$f_{v7}$	0.0638
$c_{3z}$	-26.22e-3	$J_{4xx}$	0.037	$f_{c1}$	0.245
$c_{4x}$	-1.34e-3	$J_{4xy}$	9.415e-5	$f_{c2}$	0.1523
$c_{4y}$	26.22e-3	$J_{4xz}$	3.1455e-4	$f_{c3}$	0.1827
$c_{4z}$	87.77e-3	$J_{4yy}$	0.037	$f_{c4}$	0.3591
$c_{5x}$	-0.993e-3	$J_{4yz}$	9.747e-3	$f_{c5}$	0.2669
$c_{5y}$	-111.65e-3	$J_{4zz}$	6.887e-3	$f_{c6}$	0.1658
$c_{5z}$	-26.958e-3	$J_{5xx}$	0.032	$f_{c7}$	0.2109
$c_{6x}$	-0.259e-3	$J_{5xy}$	-1.898e-4	$f_{o1}$	-0.1073
$c_{6y}$	-5.956e-3	$J_{5xz}$	-4.474e-5	$f_{o2}$	-0.1566
$c_{6z}$	-5.328e-3	$J_{5yy}$	4.945e-3	$f_{o3}$	-0.0686
$c_{7x}$	0	$J_{5yz}$	-2.023e-3	$f_{o4}$	-0.2522
$c_{7y}$	0	$J_{5zz}$	0.03	$f_{o5}$	4.53e-3
$c_{7z}$	63e-3	$J_{6xx}$	3e-3	$f_{o6}$	0.091
$J_{1xx}$	0.039	$J_{6xy}$	-2.463e-6	$f_{o7}$	-0.0127
$J_{1xy}$	3.206e-4	$J_{6xz}$	-2.323e-6	$d_1$	0.4
$J_{1xz}$	9.415e-5	$J_{6yy}$	3.068e-3	$d_2$	0.39

**Table 3.4.** Dynamic and DH parameters values used as ground-truth for the 7R KUKA LWR IV+ both with and without friction. Masses are in  $kg$ , CoMs coordinates and kinematic parameters in  $m$  and inertial parameters in  $Nm$ .

In order to make the procedure as close as possible to the reality, even in this case, all the trajectories needed for completing the steps had to respect the bounds over the positions, velocities and accelerations for all the seven joints. The real values for these symmetric limits were gathered from [5] and collected in Table 3.5.

<b>Joint <math>j</math></b>	1	2	3	4	5	6	7
$q_{\max}$ [rad]	2.9670	2.0943	2.9670	2.0943	2.9670	2.0943	2.9670
$dq_{\max}$ [rad/s]	1.7453	1.9199	1.7453	2.2689	2.2689	3.1416	3.1416
$ddq_{\max}$ [rad/s <sup>2</sup> ]	5.236	5.236	5.236	5.236	5.236	5.236	5.236

**Table 3.5.** Joint limits for the KUKA LWR IV+.

# Chapter 4

## Framework

All the code used in this work was developed through *Matlab R2019a*. In order to build the entire framework three different external toolboxes were employed:

- *Symbolic Toolbox* to build and perform computations over the dynamic models of the robots and allow to construct a dual process obtaining both numeric and symbolic quantities.
- *Global Optimization Toolbox* was used to perform the parameters extraction phase using the *simulated annealing* global optimization algorithm.
- *Communications Toolbox* was used to provide to the 3R friction model and the 7R friction model white Gaussian noise during the dynamic coefficients identification phase.

The basic structure of the framework reflects for every robot and every version, with the necessary changes. Each folder inside **Environment** represents the work done on that robot and each of these subfolders contains:

- **Data**: a folder containing all the data collected during the different phases and the information needed to perform these (e.g. bounds).
- **Framework\_dyn\_model**: a folder containing all the files for building the dynamic model of the robot using either the Lagrangian form or the Newton-Euler one.
- **Framework\_dyn\_coeff\_identification**: a folder containing all the necessary files for performing the dynamic coefficients identification, including the generation of exciting trajectories.
- **Framework\_dyn\_params\_extraction**: a folder containing all the necessary files for performing the dynamic parameters extraction phase.
- **Framework\_NE**: a folder containing all the necessary files for plotting the internal forces behaviour of the robot according to different sets of parameters.

Despite the power of the symbolic calculus provided by the symbolic toolbox, one of the main drawbacks of this tool was its slowness. Especially when working with the 7R robot, calculus can become increasingly complex: for example in order to fill the regressor and the model with the samples gathered from the trajectories for obtaining their stacked version (in the dynamic coefficients identification phase), initial time estimate suggested more than 180 hours for obtaining the solution. Very long running time required solutions for shortening these time windows: this was a very challenging problem to face. Several tricks were employed: an analysis was performed in order to select the lowest number of samples needed without affecting the

task, a 4x parallelization of the routines, another parallelization with two external devices and a decoupling/coupling modification of the code, that allowed to reduce the time needed for the above-mentioned task to almost three hours.

As a whole the framework counts more than 110 scripts and more than 410 data files collected. In Fig. 4.1 only a reduced branch for the 3R spatial frictionless manipulator of the framework is shown.

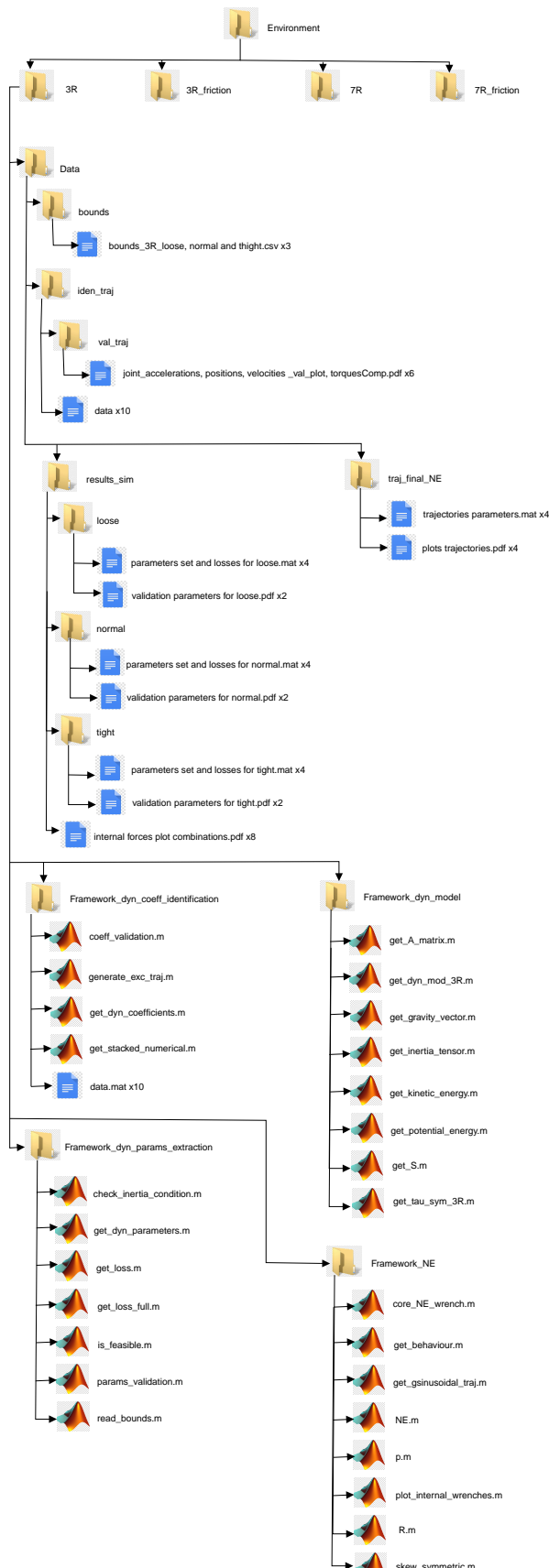


**Figure 4.1.** Partial and reduced view of the structure of the framework developed in this work. The other three branches were not depicted for the sake of clarity. General data were collected under *Data* with the multiplicity indicating the number of files presented. The logo of the folder indicates that it's a branch, the file logo that is a file with extension *.csv*, *.mat*, *.fig* or *.pdf* and the Matlab logo stands for a Matlab file (i.e. *.m*).

# Chapter 5

## Experimental Details and Results

In this chapter all the details about the implementation of the various phases will be disclosed and all the results obtained will be presented and analysed. For more technical details about the implementation, please refer to the framework attached to this report<sup>1</sup>.

### 5.1 3R Spatial Manipulator

The first robot taken into consideration in this work was the 3R spatial anthropomorphic manipulator in Fig. 3.1(a) without friction modelling. Its dynamic model was built using the symbolic Euler-Lagrangian formulation and saved in `Environment/3R/Framework_dyn_model/dyn_mod_3R.mat`. As regards the dynamic coefficients identification procedure, in order to obtain the samples needed for building the stacked version of the regressor and of the torques, three exciting trajectories were generated for each joint using the formula in Eq. (5.1) and its off-line differentiation and integration.

$$q_j(t) = \sum_{l=1}^L \frac{a_{l,j}}{lw_f} \sin(lw_f t) - \frac{b_{l,j}}{lw_f} \cos(lw_f t) + q_{0,j} \quad (5.1)$$

In this work for all the cases were used  $L = 5$  harmonics, a pulsation  $w_f$  of  $0.15\pi$  and random values of the parameters  $a$ ,  $b$ , and  $q_0$  for guaranteeing variety. The trajectories had a duration of 20 seconds and in order to have realistic simulations, the values of the joint positions, velocities and accelerations of the robot lied always inside the bounds of Table 3.3, moreover for the joint velocities and accelerations was inserted an additional side behaviour, manually computed, that allowed the trajectories to start and end to zero within a margin of 1 s. The trajectories then were sampled with a sampling rate of 0.01 that produced 2001 samples per joint per trajectory for a total of 42021 samples. Trajectories behaviour are shown in Fig. 5.1 while random parameters are collected in Table 5.1.

---

<sup>1</sup>Folder Environment.

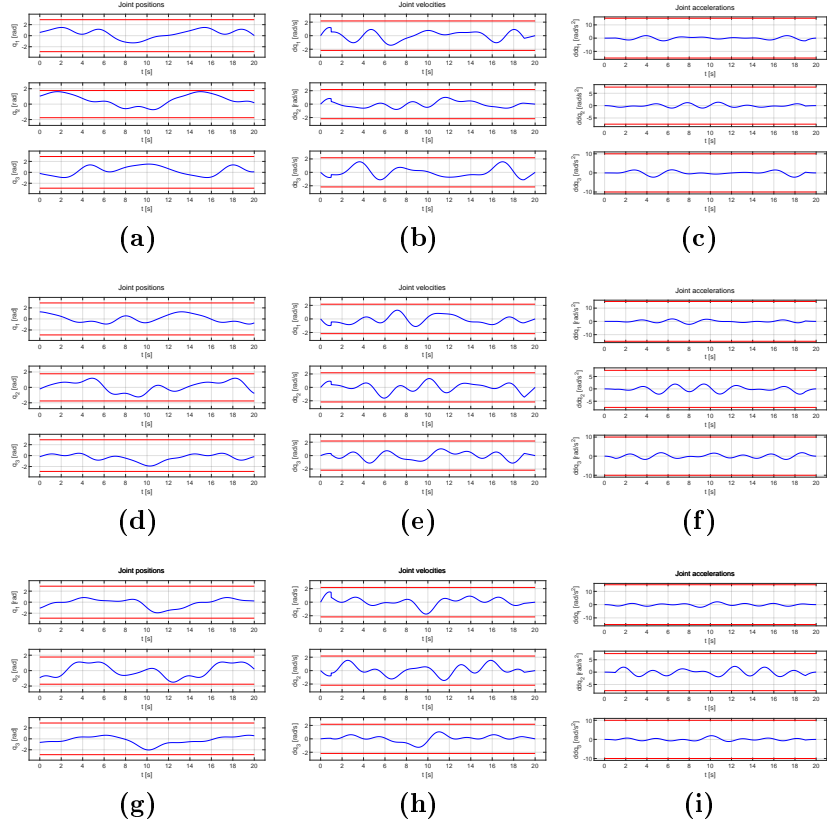


**Figure 5.1.** Trajectories used for the identification procedure of the dynamic coefficients for the 3R manipulator. (a), (b) and (c) show the first trajectory; (d), (e) and (f) the second and (g), (h) and (i) the third one. Red lines represent the joint limits.

	$a_{1,j}$	$a_{2,j}$	$a_{3,j}$	$a_{4,j}$	$a_{5,j}$	$b_{1,j}$	$b_{2,j}$	$b_{3,j}$	$b_{4,j}$	$b_{5,j}$	$q_0$
1	0.453	-0.194	0.465	-0.265	0.010	-0.209	-0.179	0.381	0.159	-0.251	0.199
2	0.402	0.182	0.061	-0.295	0.054	-0.254	-0.155	0.001	-0.085	0.244	0.390
3	-0.323	-0.450	0.118	0.313	-0.146	0.223	0.337	-0.459	0.276	-0.006	0.459
1	-0.047	0.242	-0.314	0.150	-0.116	-0.331	-0.417	-0.254	0.424	-0.279	0.069
2	0.361	-0.341	0.256	0.303	0.027	-0.085	0.214	0.119	0.446	-0.434	-0.031
3	0.351	0.246	-0.429	0.249	0.148	-0.049	-0.257	-0.068	-0.031	0.370	-0.488
1	0.318	0.364	-0.049	-0.122	0.098	0.376	0.082	-0.444	0.162	0.389	-0.258
2	0.236	-0.369	0.355	0.149	0.424	0.316	0.450	0.009	-0.400	-0.2802	-0.0960
3	0.354	-0.079	-0.353	-0.013	0.260	0.260	-0.402	0.010	0.130	0.110	-0.403

**Table 5.1.** Values of the trajectories coefficients  $A$ ,  $B$  and  $q_0$  for each joint (rows) and for each of the three trajectories used in the identification procedure (blocks of rows).

This phase of the procedure allowed the identification of 15 coefficients whose values can be seen in the Appendix A under Table A.1: in the first column there's the symbolic version of the identified coefficients, in the second their estimated numerical values, in the third the reconstructed values of the coefficients with the ground-truth parameters values and in the fourth the error between the estimated and the reconstructed values.

Finally, in order to validate these coefficients, a sinusoidal trajectory, shown in Fig. 5.2, of duration 10s was generated and sampled with a sampling rate of 0.01. Fig. 5.3 shows the

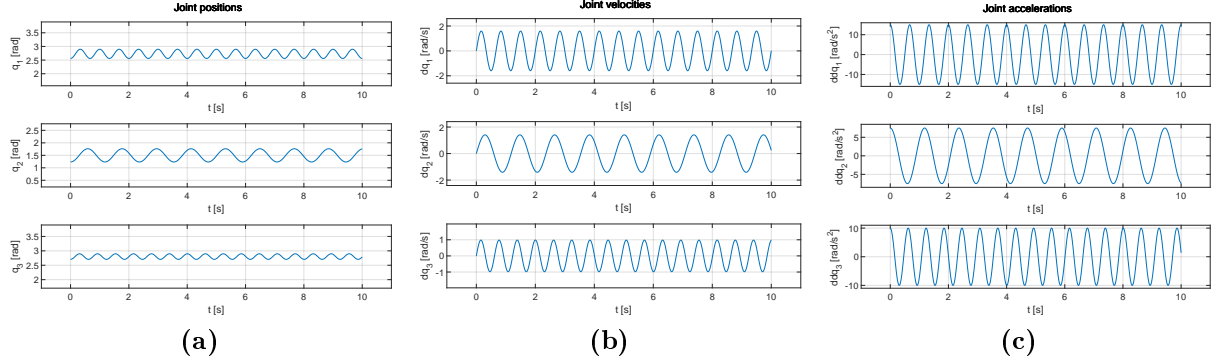


**Figure 5.2.** Trajectory for the validation of the identified coefficients for the 3R manipulator.

torques obtained with the estimated coefficients and with the real one, as it's possible to see the two behaviours are coincident.

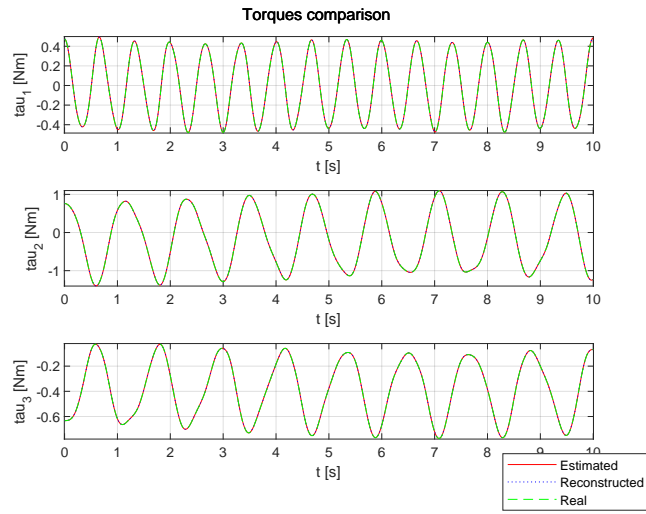


**Figure 5.3.** Torques behaviours comparisons among the one obtained with the identified coefficients (solid red line), the one obtained with the symbolic identified coefficients reconstructed (dotted blue line) and the one obtained with the real parameters inside the dynamic model (dashed green line). This comparison suggests perfect overlapping and therefore perfect identification.

The next step consisted in extracting the dynamic parameters from the set of identified coefficients through a global optimization algorithm as explained in Section 2.3 [2]. It was chosen to perform all the simulations in this work using the *simulated annealing* algorithm (i.e. `simannealbnd`) with the *Nelder-Mead* optimization as hybrid function. Others algorithm were taken into consideration, e.g. *genetic algorithm* (`ga`), but no differences were detected. Also several values where tried for the factor that increases the  $\xi$  parameters in Algorithm 1: from different constant values, to time-varying one and also a value dependent from the difference in the loss function with respect to the previous iteration. Even in these cases no relevant differences were found so it was decided to use the value in Algorithm 1. Simulations lasted for 25 iterations for each of the 30 runs in order to try to span the landscape of the problem.

As to obtain different sets of parameters, either feasible or unfeasible, and to study their degree of unfeasibility, for each manipulator and version 6 simulations were performed. In this work were used three groups of bounds: *normal* bounds, hence limits linked to the geometry of the robot, *tight* bounds hence tighter limits linked to the knowledge of the real parameters and *loose* bounds hence larger bounds that could lead to unfeasible quantities (e.g. CoMs coordinates out

of links contours). Bounds values are integrally collected in Table A.6 in the Appendix A. For each of these three bounds two simulations were performed using in the first case a loss function driven only by the internal term as in Eq. (2.28) and in the second one a full loss function with in addition the external penalties terms like total mass constraints, positive inertial tensors one and box constraints that matched the geometry of the cylindrical links.

The sets of parameters retrieved from these simulation were eventually tested to check their feasibility or the reasons of their unfeasibility. Results of this checking step are collected in Table 5.2 while for the values of the sets please refer to Table A.7 in Appendix A for their generation scenario and the paths to their values.

Set	Feasible	Unfeasible	Why
p_1		×	1 <sup>st</sup> /3 <sup>rd</sup> inertia
p_4	×		-
p_5		×	1 <sup>st</sup> inertia
p_8	×		-
p_9		×	1 <sup>st</sup> /2 <sup>nd</sup> /3 <sup>rd</sup> inertia, c <sub>1x</sub> , c <sub>1z</sub> , c <sub>3z</sub>
p_12		×	c <sub>2x</sub>

**Table 5.2.** Feasibility checking: x inertia stands for the violation of the positive definiteness of the inertia tensor for the x link;  $c_{jd}$  stands for the violation of the constraints on the CoMs coordinates: coordinate  $d$  of link  $j$  is out of bounds.

Finally all the sets of extracted parameters were validated against the ground-truth ones using a new sinusoidal trajectory. In order to produce good sinusoids that were respectful of the joint limits, some mathematical computations were performed as to obtain a wider pool of random curves through the choice of its parameters. Specifically, the velocity equation in Eq. (5.2) was off-line differentiated and integrated and the maximum and the minimum were computed giving rise to two inequalities for each quantity (i.e. position, velocity, acceleration). Then these inequalities were put in a system together with the extremes of the limits ending up in intervals for the parameters.

$$\dot{q}_i(t) = A_i \sin\left(\frac{2\pi}{T_i}t\right) \quad (5.2)$$

Results of this validation process are shown in Fig. 5.4: as it is possible to notice every set produced the right behaviour.

The last step in this process was to obtain the symbolic formulation of the internal wrenches for the manipulator and using the reference trajectory depicted in Fig. 5.5, to plot the behaviour of the internal forces acting on the joints obtained with a set of feasible parameters, an unfeasible one and the ground-truth one for all the possible combinations of these sets. Results are presented in Fig. 5.6.

As it is possible to notice of the two feasible sets  $p_4$  and  $p_8$ , the latter exhibits a more similar behaviour to the real one, especially for the third link and for the second, for which it's almost coincident. The interesting fact is that the behaviour of the unfeasible sets strongly depends on the reasons underneath their unfeasibility: when compared with the feasible and real sets, the ones that are unfeasible *only* due to inertial constraints violation, as in Fig. 5.6(a), (b), (c) and (d), have a behaviour that doesn't mirror what described in [1], in fact the internal forces trend is similar to the real one and also closer to it with respect to the feasible set one (also depending on the goodness of the feasible set).

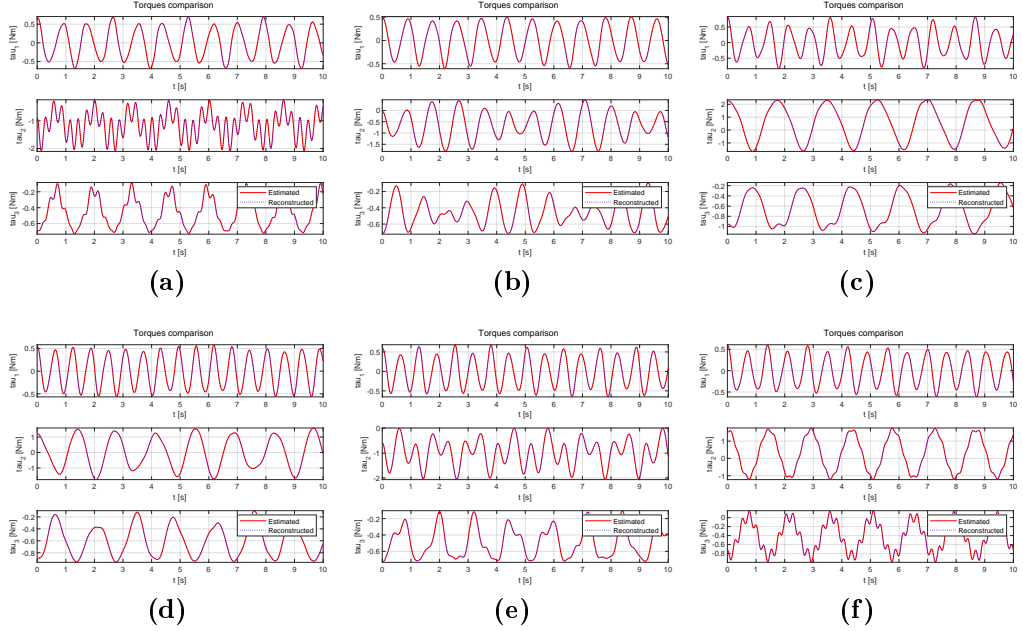


**Figure 5.4.** Comparison of torques behaviour for each joint between the real one and those obtained with the different sets of dynamic parameters: (a) Real vs.  $p_1$ ; (b) Real vs.  $p_4$ ; (c) Real vs.  $p_5$ ; (d) Real vs.  $p_8$ ; (e) Real vs.  $p_9$ ; (f) Real vs.  $p_{12}$ . For the colors representation please see the legend attached to every plot.

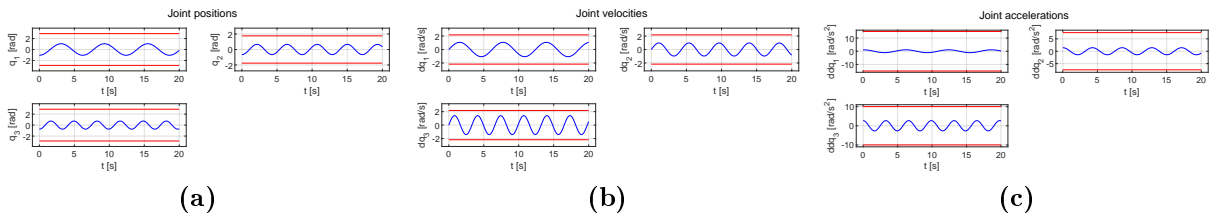


**Figure 5.5.** Reference trajectory for the internal wrenches computations for the 3R. Red lines stand for the joint limits.

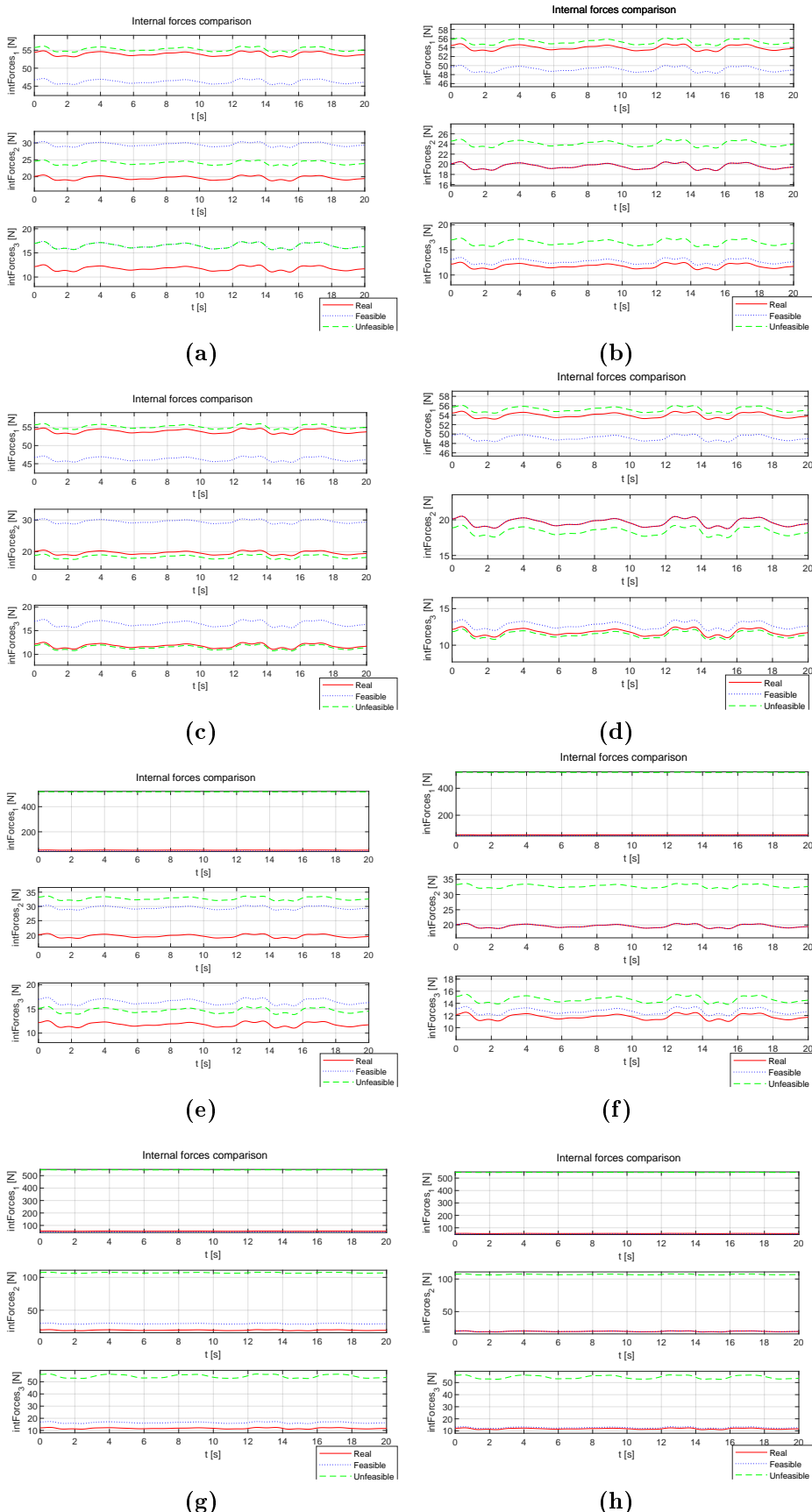


**Figure 5.6.** Comparison of internal forces behaviour for each joint among an unfeasible, feasible and the real set of dynamic parameters: (a) feasible set ( $F = p_4$ ), unfeasible set ( $UN = p_1$ ); (b)  $F = p_8$ ,  $UN = p_1$ ; (c)  $F = p_4$ ,  $UN = p_5$ ; (d)  $F = p_8$ ,  $UN = p_5$ ; (e)  $F = p_4$ ,  $UN = p_9$ ; (f)  $F = p_8$ ,  $UN = p_9$ ; (g)  $F = p_4$ ,  $UN = p_{12}$ ;  $F = p_8$ ,  $UN = p_{12}$ . For the colors representation please see the legend attached to every plot.

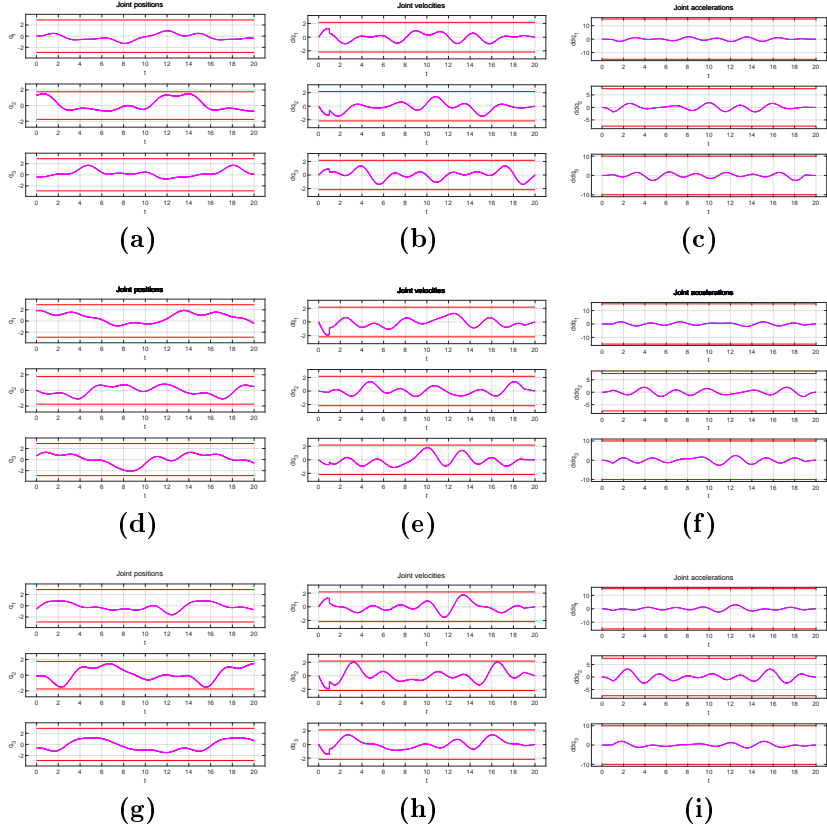


**Figure 5.7.** Trajectories used for the identification procedure of the dynamic coefficients for the 3R manipulator with friction. (a), (b) and (c) show the first trajectory; (d), (e) and (f) the second and (g), (h) and (i) the third one. Red lines represent the joint limits, the blue line is the trajectory while the pink one is the trajectory corrupted by the noise.

On the other hand, when the set is unfeasible due to *only* CoMs constraints violation, the results are similar to those shown in [1], as depicted in Fig. 5.6(g) and (h): in fact the unfeasible set differs from the real-feasible pairs of an order of at least  $5e+1$  to  $5e+2$  N.

In case in which a set is unfeasible due for the violation of inertial *and* CoMs constraints, the behaviour of the set is almost unpredictable, such as in Fig. 5.6(e) and (f), from the [1] trend (e.g. strong for the first link) to very close to the real one (e.g. for the third link).

## 5.2 3R Spatial Manipulator with Friction Model and Gaussian Noise

The entire procedure was then applied again to the 3R spatial anthropomorphic manipulator of Fig. 3.1(a) but modelling the friction phenomena as in Eq. (2.16). The dynamic model of this manipulator was again computed using the Euler-Lagrangian formulation augmented with the torque produced by the friction and saved in `Environment/3R_friction/Framework_dyn_model/dyn_mod_3R_friction.mat`.

For identifying the dynamic coefficients were again generated *three* exciting trajectories, like in Section 5.1, whose behaviour is depicted in Fig. 5.7 and whose parameters are not shown for brevity. With the same setting of Section 5.1, 42021 samples where collected. In order to increase the realism of this identification procedure a White Gaussian Noise process (AWGN) with a *signal-to-noise ratio* (SNR) of 30 dB was added to the identification trajectories (pink line in Fig. 5.7).

At the end of this step 24 dynamic coefficients were identified whose symbolic formulation is

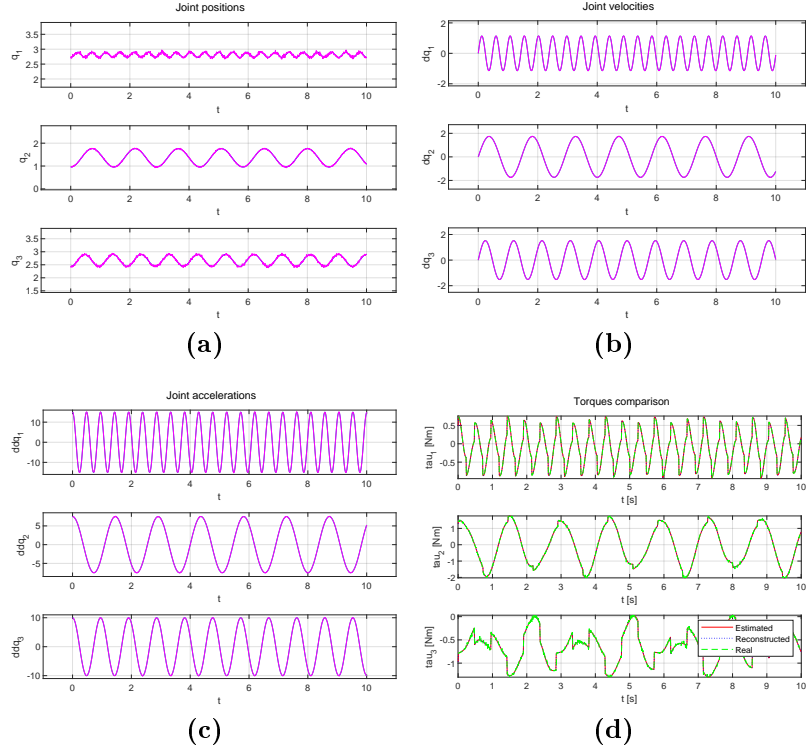


**Figure 5.8.** (a), (b), (c) Trajectory used for validating the dynamic coefficients identified in the 3R with friction; (d) torques behaviours comparisons among the one obtained with the identified coefficients (solid red line), the one obtained with the symbolic identified coefficients reconstructed (dotted blue line) and the one obtained with the real parameters inside the dynamic model (dashed green line).

reported in the first column of Table A.2 in Appendix A, while in the second one there are the numerical estimated values, in the third the reconstructed one and in the last the identification error.

Finally the coefficients where validated using the sinusoidal trajectory in Fig. 5.8(a), (b) and (c) overlapped to another AWGN process with SNR = 40 dB producing the coincident torques in Fig. 5.8(d).

The parameters extraction phase had a similar structure of Section 5.1, namely three bounds, i.e. normal, tight and loose, with two different loss functions each (i.e. only internal loss and full, hence internal and external constraints). Bounds values are again collected in Table A.6. The obtained sets of dynamic parameters are presented in Table A.8 along with the setting behind their generation and the paths for seeing their values. The results of the feasibility check are shown in Table 5.3.

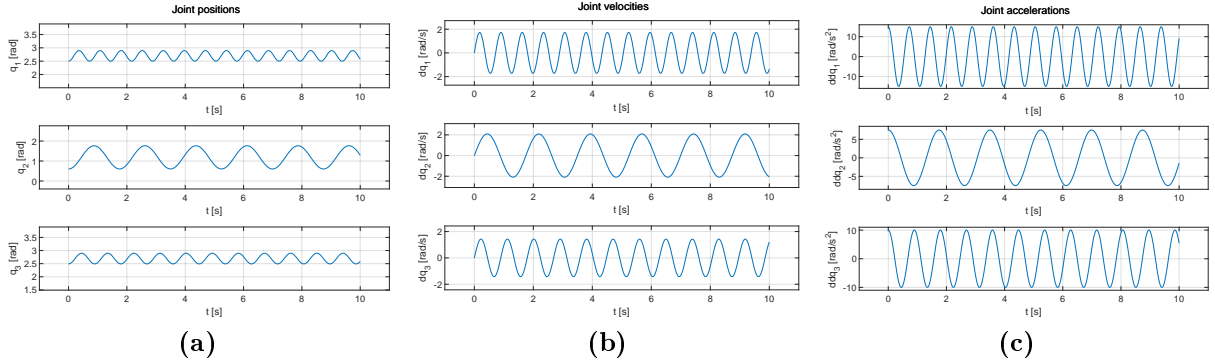


**Figure 5.9.** Trajectory used for the validation of the sets of parameters extracted for the 3R robot with friction.

Set	Feasible	Unfeasible	Why
p_13		×	1 <sup>st</sup> inertia
p_16	×		-
p_17		×	1 <sup>st</sup> inertia
p_20	×		-
p_21		×	1 <sup>st</sup> /3 <sup>rd</sup> inertia, c <sub>1x</sub> , c <sub>1z</sub> , c <sub>2x</sub> , c <sub>2z</sub> , c <sub>3z</sub>
p_24		×	c <sub>1x</sub> , c <sub>2x</sub>

**Table 5.3.** Feasibility checking: x inertia stands for the violation of the positive definiteness of the inertia tensor for the x link;  $c_{jd}$  stands for the violation of the constraints on the CoMs coordinates: coordinate  $d$  of link  $j$  is out of bounds.

These parameters were validated with a new sinusoidal trajectory as in Section 5.1 whose trend is depicted in Fig. 5.9, while the results of the validation are shown in Fig. 5.10. As it's possible to notice the trends overlap.

Finally the internal forces behaviour were computed using the sinusoidal trajectory in Fig. 5.11 obtaining the plots in Fig. 5.12.

As it's possible to notice of the two feasible sets, i.e.  $p_{16}$  and  $p_{20}$ , the latter produced a closer behaviour to the real one than the former. For the unfeasible sets due to the violation of *only* inertial constraints like in Fig. 5.12(a), (b), (c) and (d), the unfeasible trend differ from the real one but not for high order (in some cases even closer than the feasible one). For unfeasible set due to the violation of *only* CoMs constraints, as in Fig. 5.12(g) and (h), the difference is very accentuated while for the others due to *mixed* types of constraints violation, i.e. Fig. 5.12(e) and (f), the behaviour is unpredictable, either very far from the real one, as in paper [1], or not so different (e.g. third link).

### 5.3 KUKA LWR IV+ 7R

The second manipulator taken into consideration in this work was the 7R KUKA LWR IV+ of Fig. 3.2(a). The entire process was performed also for this robot, with the same modalities described in Section 5.1 with the appropriate augmentations. Deal with this huge robot was extremely challenging since its complexity required a careful and long analysis to understand potential inaccuracies and very stretched execution time windows and very demanding computational resources. Thanks to the high parallelization technique introduced in Chapter 4, the requirements

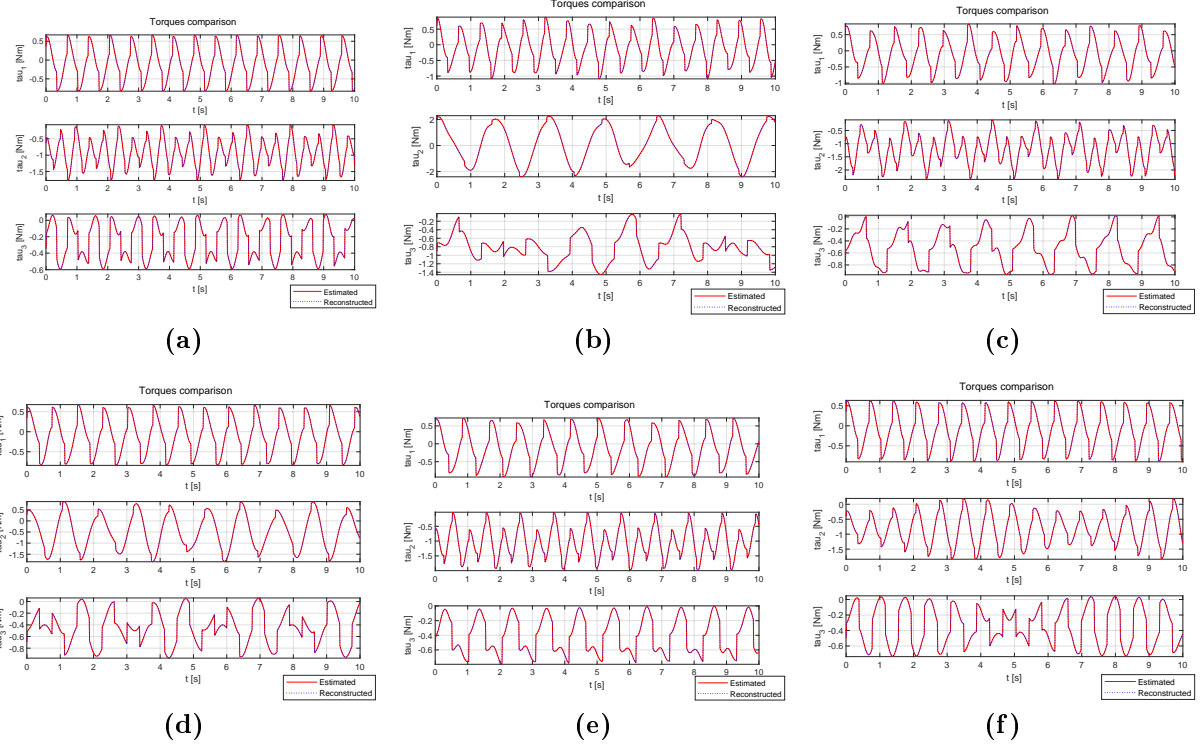


**Figure 5.10.** Comparison of torques behaviour for each joint between the real one and those obtained with the different sets of dynamic parameters: (a) Real vs.  $p_{13}$ ; (b) Real vs.  $p_{16}$ ; (c) Real vs.  $p_{17}$ ; (d) Real vs.  $p_{20}$ ; (e) Real vs.  $p_{21}$ ; (f) Real vs.  $p_{24}$ . For the colors representation please see the legend attached to every plot.

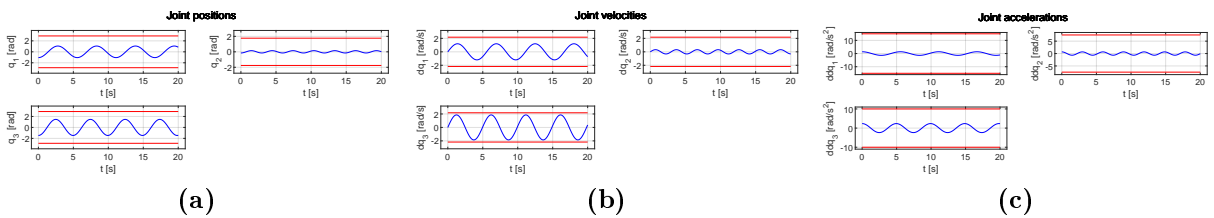


**Figure 5.11.** Reference trajectory for the internal wrenches computations for the 3R with friction. Red lines stand for the joint limits.

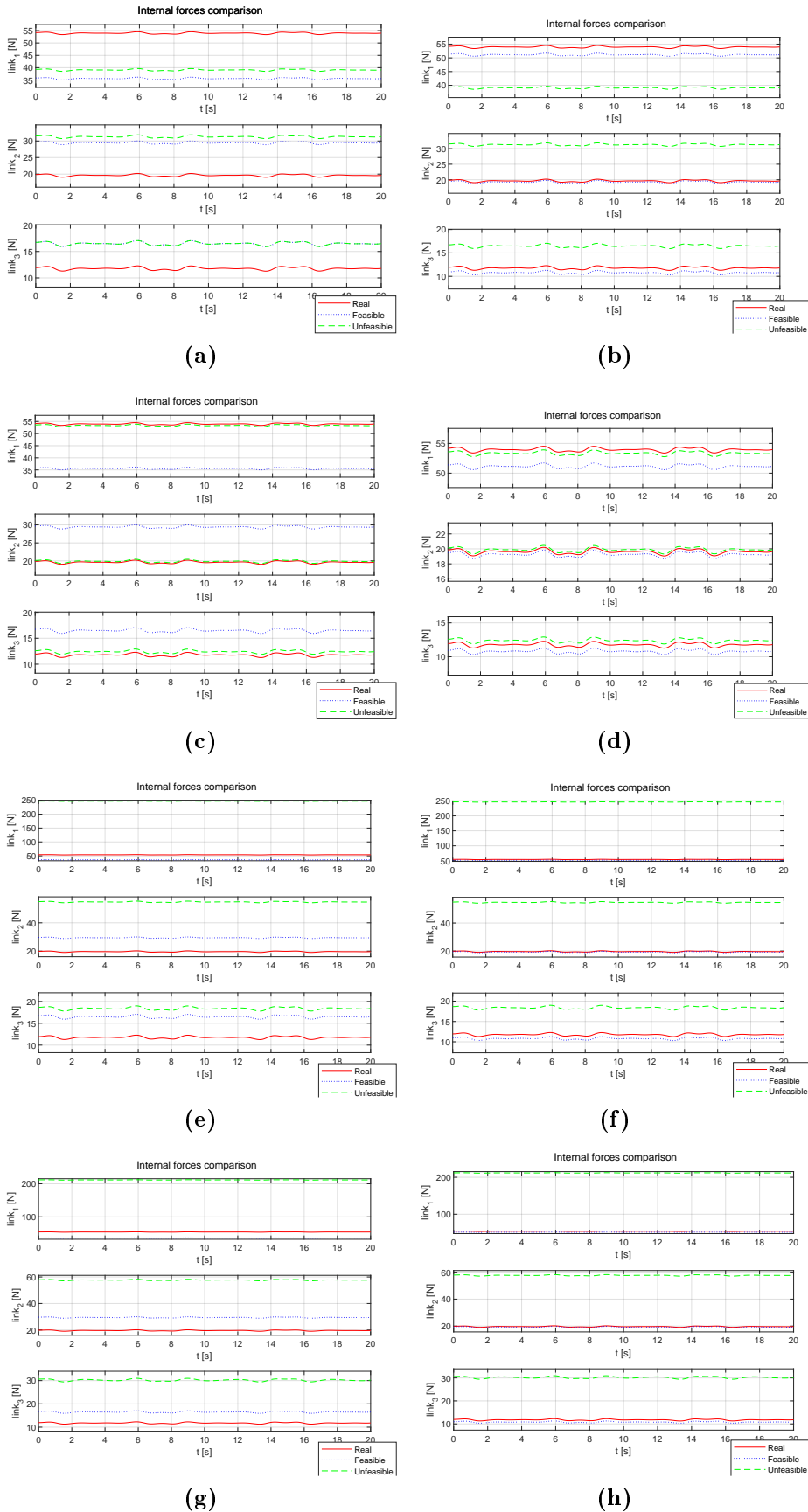


**Figure 5.12.** Comparison of internal forces behaviour for each joint among an unfeasible, feasible and the real set of dynamic parameters: (a) feasible set ( $F = p_{16}$ ), unfeasible set ( $UN = p_{13}$ ); (b)  $F = p_{20}$ ,  $UN = p_{13}$ ; (c)  $F = p_{16}$ ,  $UN = p_{17}$ ; (d)  $F = p_{20}$ ,  $UN = p_{17}$ ; (e)  $F = p_{16}$ ,  $UN = p_{21}$ ; (f)  $F = p_{20}$ ,  $UN = p_{21}$ ; (g)  $F = p_{16}$ ,  $UN = p_{24}$ ;  $F = p_{20}$ ,  $UN = p_{24}$ . For the colors representation please see the legend attached to every plot.

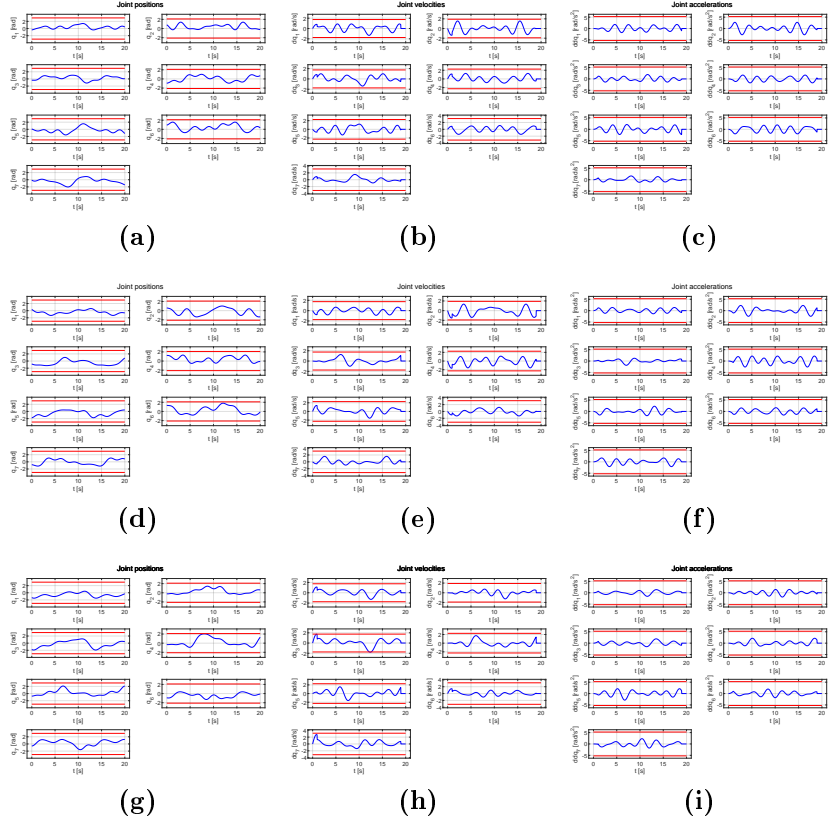


**Figure 5.13.** Trajectories used for the identification procedure of the dynamic coefficients for the 7R manipulator. (a), (b) and (c) show the first trajectory; (d), (e) and (f) the second and (g), (h) and (i) the third one. Red lines represent the joint limits.

were drastically reduced still remaining very demanding, in fact, as already mentioned in Section 2.1, it was necessary to build the dynamic model using the recursive Newton-Euler routine. The process identification phase was performed using *three* exciting trajectories, generated using the Eq. (5.1) as in Section 5.1 whose plots are shown in Fig. 5.13 while their parameters are not shown for brevity. Even if the duration of the trajectory remained 20s, the sampling rate was 0.034 allowing the collection of 12327 samples.

This procedure provided 43 coefficients, collected in the symbolic, numerical and reconstructed form in Table A.3 in the Appendix A, along with their estimation error.

The identified coefficients were then validated using the sinusoidal trajectory in Fig. 5.14(a), (b) and (c) obtaining the equivalent behaviour, to the real one, of the torques generated, as shown in Fig. 5.14(d). This means a perfect identification.

The dynamic parameters extraction phase was performed as in Section 5.1 but with 35 iterations per run and 50 runs. The bounds used in these simulations are integrally collected in the Appendix A in Table A.5 while the sets of dynamic parameters extracted are presented in Table A.9 in the Appendix A along with the paths to their values. Again for each group of bounds two simulations were performed using only the internal loss or using the full loss (hence with external terms). In this last case box inequalities for the CoMs constraints were again employed due to the non-convex shape of the links. In addition, since the last links of the robot form a sphere it was possible to choose a spheric parametrization of the boundaries to compute the loss but no relevant difference was found with respect to using box inequalities also for these links.

The sets were then checked to prove their feasibility obtaining Table 5.4 and validated using a sinusoidal trajectory ending up in the confirm of having extracted good sets of parameters. For the sake of brevity and compactness, results of these validations are not shown.

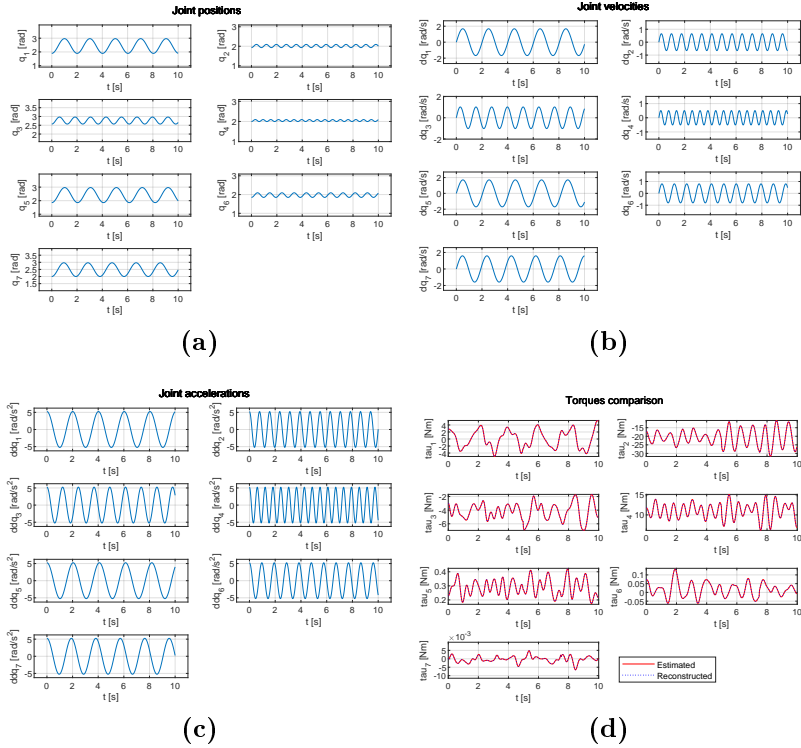


**Figure 5.14.** (a), (b), (c) Trajectory used for validating the dynamic coefficients identified in the 7R; (d) torques behaviours comparisons among the one obtained with the identified coefficients (solid red line), the one obtained with the symbolic identified coefficients reconstructed (dotted blue line) and the one obtained with the real parameters inside the dynamic model (dashed green line).

Set	Feasible	Unfeasible	Why
p_25		×	1 <sup>st</sup> /3 <sup>rd</sup> /4 <sup>th</sup> /5 <sup>th</sup> /7 <sup>th</sup> inertia
p_28	×		-
p_29		×	1 <sup>st</sup> /3 <sup>rd</sup> /6 <sup>th</sup> /7 <sup>th</sup> inertia, $c_{7z}$
p_32	×		$c_{7z}$
p_33	×		1 <sup>st</sup> /3 <sup>rd</sup> /6 <sup>th</sup> /7 <sup>th</sup> inertia, $c_{1x}$ , $c_{2y}$ , $c_{3y}$ , $c_{5y}$ , $c_{6z}$ , $c_{7z}$
p_36	×		$c_{1x}$ , $c_{2y}$ , $c_{2z}$ , $c_{3y}$ , $c_{4y}$ , $c_{6y}$ , $c_{7z}$

**Table 5.4.** Feasibility checking: x inertia stands for the violation of the positive definiteness of the inertia tensor for the x link;  $c_{jd}$  stands for the violation of the constraints on the CoMs coordinates: coordinate  $d$  of link  $j$  is out of bounds.

Finally with the sinusoidal trajectory in Fig. 5.15 was possible to plot the behaviour of the internal forces acting on the seven links obtaining Fig. 5.16.

As it's possible to notice the only obtained feasible set of parameters was  $p_{28}$ : the behaviour of the internal forces according to this set is anyway not enough close to the real one, with the exception of the last link. As regards the unfeasible sets, with the increased number of parameters, their behaviour changed remaining interesting. Situations in which the set is unfeasible due to *only* inertial constraints violation *or* in which again inertial constraints were violated *and* very few CoMs coordinates were out of bounds (e.g. 1/21), as in Fig. 5.16 (a), (b) and (c), the behaviour of the internal forces doesn't differ in a strong fashion from the real one (in some cases is even closer with respect to the feasible set). However, the difference is

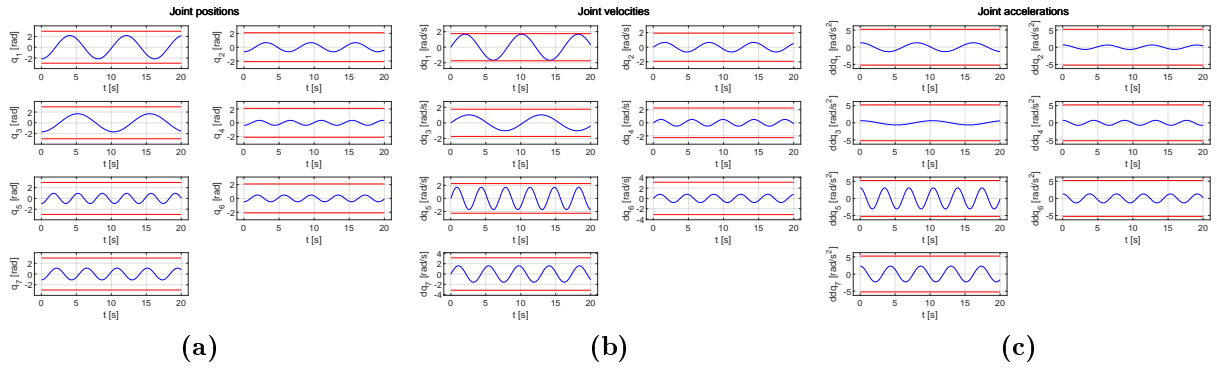


**Figure 5.15.** Reference trajectory for the internal wrenches computations for the 7R. Red lines stand for the joint limits.

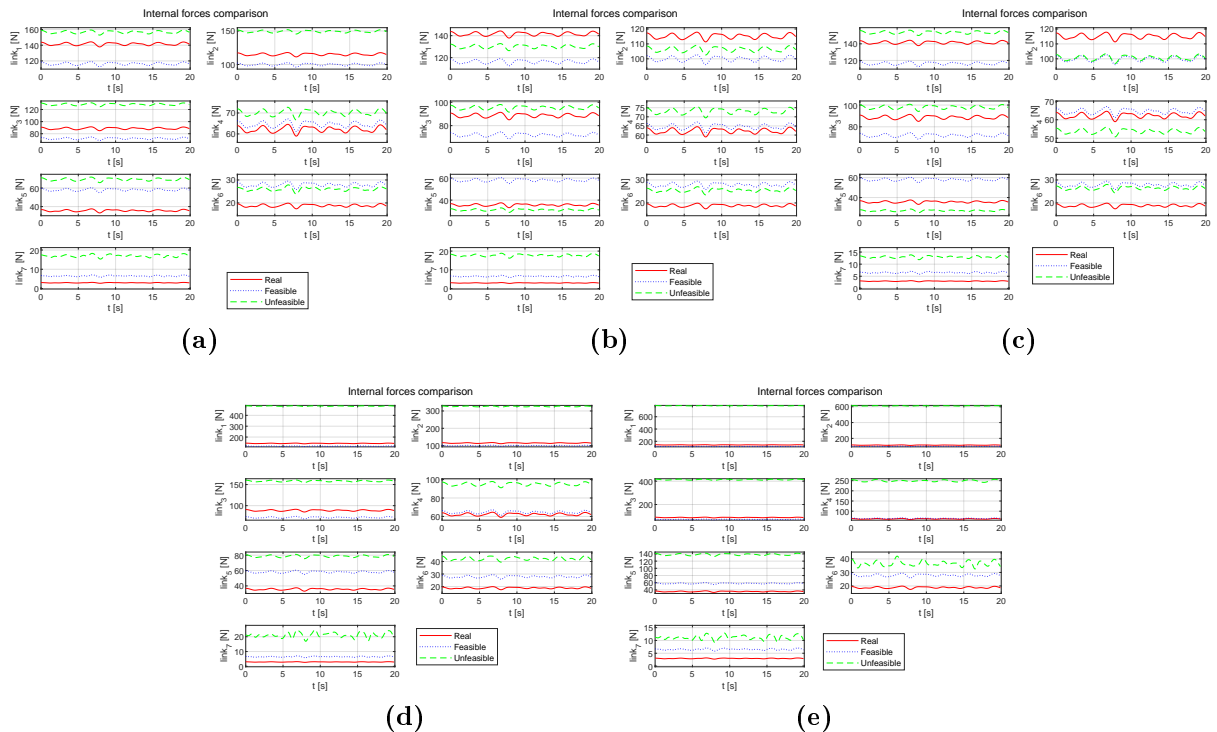


**Figure 5.16.** Comparison of internal forces behaviour for each joint among an unfeasible, feasible and the real set of dynamic parameters: (a) feasible set ( $F$ ) =  $p_{28}$ , unfeasible set ( $UN$ ) =  $p_{25}$ ; (b)  $F = p_{28}$ ,  $UN = p_{29}$ ; (c)  $F = p_{28}$ ,  $UN = p_{32}$ ; (d)  $F = p_{28}$ ,  $UN = p_{33}$ ; (e)  $F = p_{28}$ ,  $UN = p_{36}$ . For the colors representation please see the legend attached to every plot.

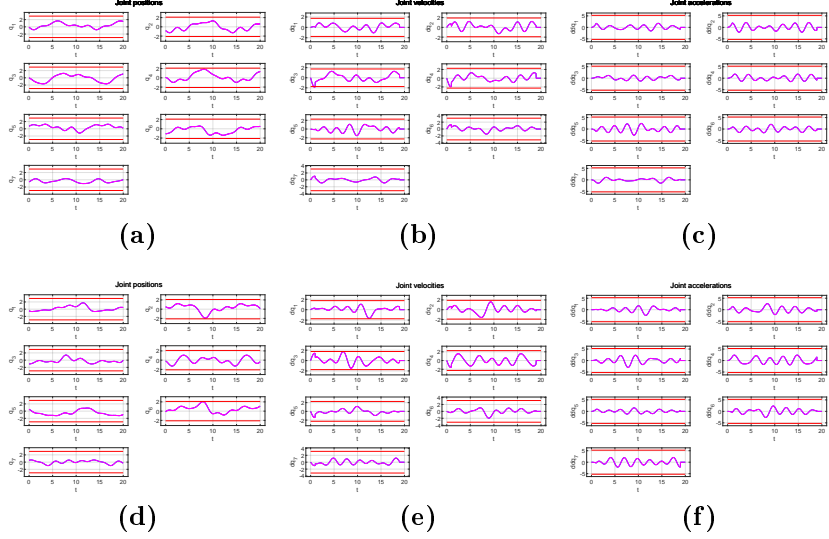


**Figure 5.17.** Trajectories used for the identification procedure of the dynamic coefficients for the 7R manipulator with friction. (a), (b) and (c) show the first trajectory; (d), (e) and (f) the second one. Red lines represent the joint limits, the blue line is the trajectory while the pink one is the trajectory corrupted by the noise.

more appreciable on the link that possesses the CoM violation. In cases in which the number of CoMs constraints violated increased, *even with* inertial violations, such as Fig. 5.16(d) and (e), the behaviour shown in [1] becomes more visible with differences with respect to the real trend of the order from  $2e + 1$  to  $5e + 2$  N.

## 5.4 KUKA LWR IV+ 7R with Friction Model and Gaussian Noise

The last version addressed in this work was the 7R KUKA LWR IV+ (Fig. 3.2(a)) augmented with friction model as in Eq. (2.16).

As in Section 5.3, the dynamic model of the manipulator was computed using the Newton-Euler formulation appropriately augmented to handle the friction phenomena. The identification procedure of the dynamic coefficients provided 64 regroups of parameters collected in the Appendix A in Table A.4 with the usual structure of symbolic-estimated-reconstructed-error. As it's possible to notice coefficients were estimated very precisely thanks to *two* trajectories, reported in Fig. 5.17, sampled with a sampling rate of 0.034 and corrupted with a AWGN process with SNR of 30dB. 8218 samples were collected.

The identified coefficients were then validated using the sinusoidal trajectory in Fig. 5.18(a), (b) and (c) while in (d) is shown the torques comparison that confirmed the good identification. In order to extract the sets of dynamic parameters, six simulations were performed on this robot, with the same settings of 5.3. Bounds are again reported in Table A.5, parameters sets explained in Table A.10 both in the Appendix A and feasibility check results in Table 5.5.

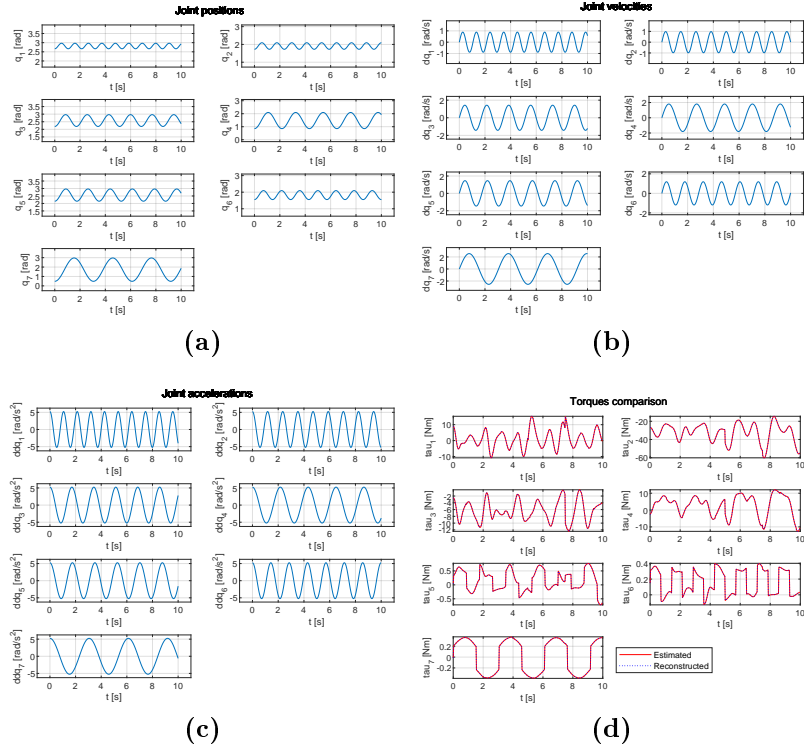


**Figure 5.18.** (a), (b), (c) Trajectory used for validating the dynamic coefficients identified in the 7R with friction modelling; (d) torques behaviours comparisons among the one obtained with the identified coefficients (solid red line), the one obtained with the symbolic identified coefficients reconstructed (dotted blue line) and the one obtained with the real parameters inside the dynamic model (dashed green line).

Set	Feasible	Unfeasible	Why
p_37			1 <sup>st</sup> /3 <sup>rd</sup> /5 <sup>th</sup> /6 <sup>th</sup> /7 <sup>th</sup> inertia
p_40	×		-
p_41		×	1 <sup>st</sup> /3 <sup>rd</sup> /5 <sup>th</sup> /6 <sup>th</sup> /7 <sup>th</sup> inertia
p_44	×		-
p_45		×	1 <sup>st</sup> /3 <sup>rd</sup> /4 <sup>th</sup> /5 <sup>th</sup> /6 <sup>th</sup> /7 <sup>th</sup> inertia
p_48	×		-

**Table 5.5.** Feasibility checking: x inertia stands for the violation of the positive definiteness of the inertia tensor for the x link;  $c_{jd}$  stands for the violation of the constraints on the CoMs coordinates: coordinate  $d$  of link  $j$  is out of bounds.

Validation of extracted parameters were performed using a sinusoidal trajectory but for the sake of brevity results are not shown.

The final step in this work was to plot the internal forces acting on the links for the retrieved sets of dynamic parameters. The results of all the combinations of feasible-unfeasible sets are reported in Fig. 5.19<sup>2</sup>.

As it's possible to notice three sets of feasible parameters were obtained:  $p_{40}$ ,  $p_{44}$  and  $p_{48}$ . The last one provided closer behaviour with respect to the real one. From Table 5.5 it was seen that the unfeasible sets are unfeasible due to the same reasons (only inertial violations: one of the sets has an additional inertia tensor not positive definite). This opened the possibility of

<sup>2</sup>For brevity the sinusoidal trajectory used to produce those internal behaviours is not reported.

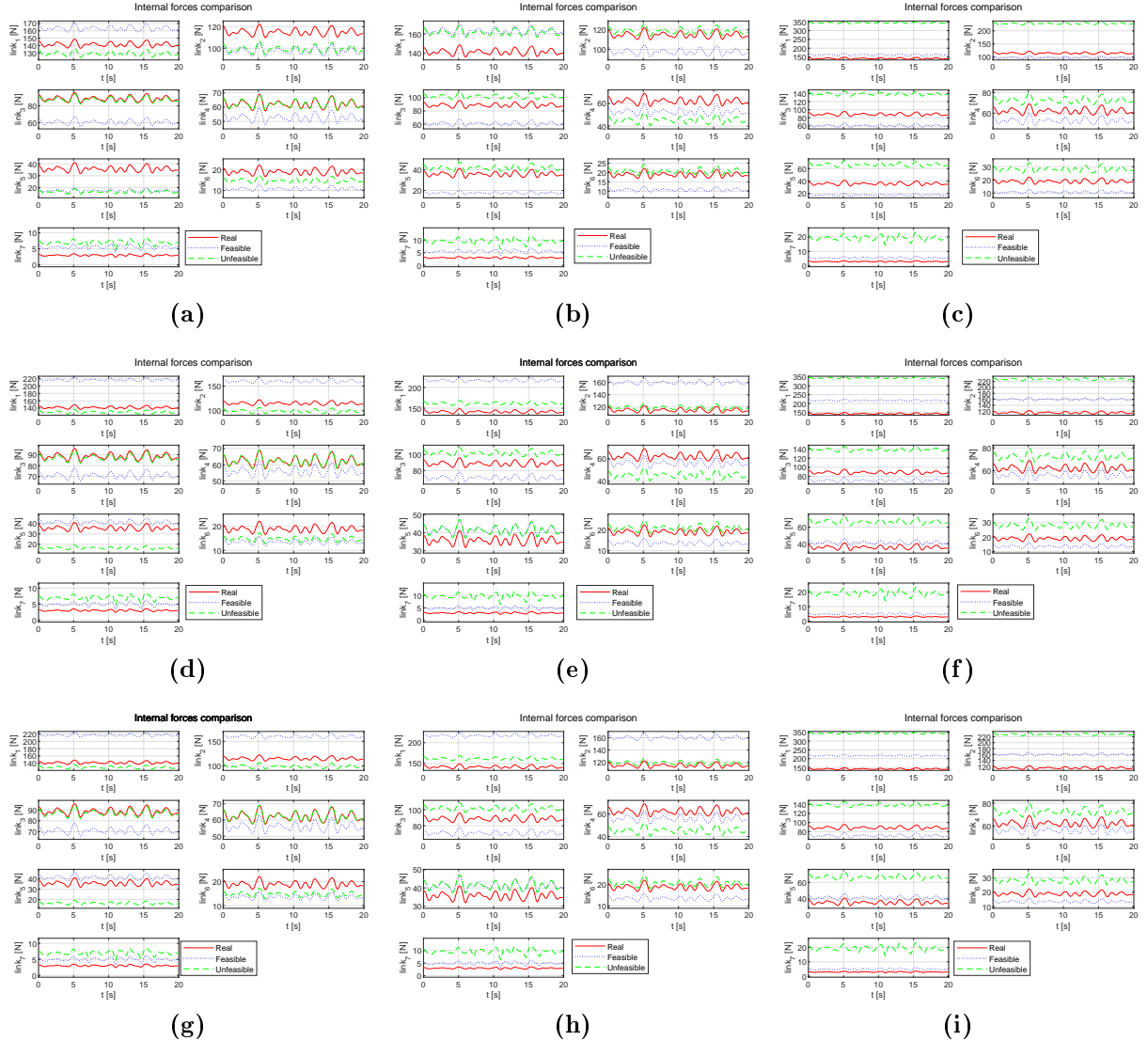


**Figure 5.19.** Comparison of internal forces behaviour for each joint among an unfeasible, feasible and the real set of dynamic parameters: (a) feasible set ( $F = p_{40}$ ), unfeasible set ( $UN = p_{37}$ ); (b)  $F = p_{40}$ ,  $UN = p_{41}$ ; (c)  $F = p_{40}$ ,  $UN = p_{45}$ ; (d)  $F = p_{44}$ ,  $UN = p_{37}$ ; (e)  $F = p_{44}$ ,  $UN = p_{41}$ ; (f)  $F = p_{44}$ ,  $UN = p_{45}$ ; (g)  $F = p_{48}$ ,  $UN = p_{37}$ ; (h)  $F = p_{48}$ ,  $UN = p_{41}$ ; (i)  $F = p_{48}$ ,  $UN = p_{45}$ . For the colors representation please see the legend attached to every plot.

investigating how being different sets would affect the internal forces behaviour with respect to being unfeasible for the same reasons. Despite the diversity of the parameters sets, as it's possible to notice being unfeasible for the same reasons doesn't strongly affect the behaviour of the internal forces, however, adding more reasons to the unfeasibility check can lead to very different results with the appearance of extreme behaviour of the nature of those in [1].

# Chapter 6

## Conclusions

In this work were highlighted the differences among the behaviours of the internal forces acting on the links produced by feasible and unfeasible sets of dynamic parameters. More specifically, the dynamic model for each manipulator taken into consideration was derived and its dynamic coefficients were identified through the use of exciting trajectories respectful of the joint limits. Then its dynamic parameters were extracted using a global optimization algorithm and a loss function composed by an internal term and an external one based on the degree of violation of feasibility constraints. Finally the trends of the internal forces were retrieved and plotted. The entire procedure was performed on a 3R spatial anthropomorphic manipulator, this 3R with friction modelling, the 7R KUKA LWR IV+ and this 7R with friction modelling.

This work is based on the procedure described in [1], aimed at analysing the results of the internal forces acting on the links, not only at the with respect to feasible or unfeasible dynamic parameters, but differentiating within the latter category to try to understand how the *degree* of unfeasibility could affect the above mentioned internal trend.

It was discovered that for robots with few links (e.g. 3R manipulators), the behaviour of the internal forces was unpredictable: from being pretty close to the real one to highly different from it as in [1] based on the fact that only inertial or mixed inertial-CoMs constraints were violated for the former or that only the CoMs were violated for the latter. When the number of links grows, as in the 7Rs, the behaviour changes and also the number of violated CoMs constraints seems to affect the trends. In addition it was possible to study how being different parameters sets but with the same reasons of unfeasibility reflected on the internal behaviour. It was found that more simulations were needed as to support and better formulate these theories.

As regards the comparison between feasible and unfeasible sets, it was shown that this relation is strongly dependent on the choice of the former: some sets matched very closely the real behaviour, while others differ significantly. This suggested that, as future work, it might be possible to investigate also the degree of feasibility, differentiating between the sets that are firmly feasible and those that are closer to the limit of unfeasibility. In the same way it will be possible to expand more the unfeasibility study not only limiting at checking the comparisons at the *reason* level but also at the *degree of reason*: some sets are unfeasible only due to very small violations, hence almost feasible, while others are strongly unfeasible.

Finally, this work could be extended by testing the whole procedure with a *payload* for studying how it may affect the internal forces behaviour. In this work only an initial coefficients identification phase for a symmetric payload attached to the end-effector of the 3R was performed [4].

# Appendix A

## Supplementary Material

Coefficient	Estimated	Real	Error
$44.44*J3zz - 20.66*J2zz + m2$	0.9236	0.9235	-0.3453e-13
$m3 - 44.44*J3zz$	0.7996	0.7995	-0.3242e-13
$4.545*J2zz + m2*c2x$	-0.00949	-0.00949	0.0102e-13
$m2*c2y$	0.000799	0.0008	0.0005e-13
$6.667*J3xz - 4.545*J2xz + m2*c2z$	0.002965	0.00296	-0.0042e-13
$6.667*J3zz + m3*c3x$	-0.0119	-0.0119	0.0013e-13
$m3*c3y$	0.0024	0.0024	0.0009e-13
$m3*c3z - 6.667*J3xz$	0.00108	0.00108	0.0108e-13
$J1yy + J2yy + J3yy - J2zz - J3zz$	0.026310	0.02631	-0.0153e-13
$J2xx - J2yy + J2zz$	0.0004979	0.000498	-0.0081e-13
$J2xy$	0.0001269	0.000127	-0.0093e-13
$J2yz$	-3.200e-06	-3.2e-06	0.0069e-13
$J3xx - J3yy + J3zz$	0.0005609	0.000561	-0.0071e-13
$J3xy$	0.000252	0.000252	0.0044e-13
$J3yz$	-1.440e-05	-1.44e-05	0.0038e-13

**Table A.1.** The fist column represents the symbolic version of the retrieved dynamic parameters for the 3R, the second column is the estimated numerical value, the third the real one obtained with the ground-truth parameters while the last column is the identification error.

Coefficient	Estimated	Real	Error
fv1	0.0665	0.0665	0.0008e-13
fv2	0.1987	0.1987	0
fv3	0.0399	0.0399	0.0162e-13
fc1	0.2450	0.2450	0.0006e-13
fc2	0.1523	0.1523	0.0031e-13
fc3	0.1827	0.1827	-0.0133e-13
fo1	-0.1073	-0.1073	-0.0011e-13
fo2	-0.1566	-0.1566	0.0275e-13
fo3	-0.0686	-0.0686	-0.0017e-13

**Table A.2.** The fist column represents the symbolic version of the retrieved dynamic friction parameters for the 3R with friction, the second column is the estimated numerical value, the third the real one obtained with the ground-truth parameters while the last column is the identification error. All the 24 coefficients were identified but the first 15 were equal to those identified in the vanilla 3R hence for the ease of reading only the new one were reported here.

Coefficient	Estimated	Values	Error
6.25*J2yy - 0.6575*J4yy +			
+ 6.25*J3zz - 0.6575*J5zz +	5.2102	5.2102	9.14e-14
+ m3 + m4 - 5*m3*c3y - 5.1282*m5*c5y			
0.6575*J4yy + 6.5746*J5zz +	3.0671	3.0671	-1.55e-14
+ m5 + m6 + m7 + 5.1282*m5*c5y			
m2*c2x	0.00361	0.003618	-2.59e-15
m2*c2z - 2.5*J3zz - 2.5*J2yy + m3*c3y	0.2890	0.2890	-1.88e-14
m3*c3x	-0.003618	-0.003618	1.64e-15
m3*c3z + m4*c4y	-2.498e-15	0	2.49e-15
m4*c4x	-0.003618	-0.003618	2.06e-15
m4*c4z - 2.5641*J5zz - 2.5641*J4yy - m5*c5y	0.2550	0.2550	5.44e-15
m5*c5x	-0.001688	-0.00168	-1.12e-16
m5*c5z - m6*c6y	-0.03629	-0.0362	-1.44e-15
m6*c6x	-0.0004143	-0.0004144	-4.90e-16
m6*c6z + m7*c7z	0.01037	0.01037	-9.59e-16
m7*c7x	-2.1926e-15	0	2.19e-15
m7*c7y	1.4502e-15	0	-1.45e-15
J1yy + J2zz	0.0137	0.013774	2.15e-15
J2xx - J2yy - J2zz	-0.00486	-0.004867	-5.81e-15
J2xy	9.415e-05	9.415e-05	-6.56e-15
J2xz	-0.000314	-0.0003145	3.32e-15
J2yz	0.00974	0.009747	8.41e-16
J3xx - J3zz + J4zz	-0.02322	-0.023226	-3.35e-15
J3xy	0.0003144	0.0003145	2.39e-15
J3xz	-9.557e-05	-9.5572e-05	-3.36e-15
J3yy + J4zz	0.013774	0.0137742	2.61e-16
J3yz	0.0026809	0.002681	2.88e-16
J4xx - J4yy - J4zz	-0.0068869	-0.006887	-1.91e-15
J4xy	9.415e-05	9.415e-05	-2.02e-16
J4xz	0.000314549	0.00031455	5.86e-16
J4yz	0.00974699	0.009747	1.61e-16
J5xx - J5zz + J6zz	0.0054700	0.00547	-1.4e-15
J5xy	-0.000189	-0.0001898	-7.2e-17
J5xz	-4.474e-05	-4.474e-05	1.01e-15
J5yy + J6zz	0.0084150	0.008415	-1.97e-15
J5yz	-0.0020230	-0.002023	1.27e-15
J6xx + J7yy - J6zz	0.0008219	0.000822	2.67e-15
J6xy	-2.463e-06	-2.463e-06	1.74e-16
J6xz	-2.323e-06	-2.323e-06	1.06e-15
J6yy + J7yy	0.00436	0.00436	-1.58e-15
J6yz	-7.01e-05	-7.008e-05	-2.21e-16
J7xx - J7yy	0.00217	0.002178	-3.46e-16
J7xy	-2.081e-16	0	2.08e-16
J7xz	-9.714e-16	0	9.71e-16
J7yz	5.689e-16	0	-5.68e-16
J7zz	0.0001583	0.0001584	7.74e-16

**Table A.3.** The fist column represents the symbolic version of the retrieved dynamic parameters for the 7R, the second column is the estimated numerical value, the third the real one obtained with the ground-truth parameters while the last column is the identification error.

Coefficient	Estimated	Values	Error
fv1	0.0665	0.0665	-3.3584246494911e-15
fv2	0.1987	0.1987	-1.25455201782643e-14
fv3	0.0399	0.0399	-6.03683769639929e-16
fv4	0.2256	0.2257	6.66133814775094e-16
fv5	0.1023	0.1023	-3.1641356201817e-15
fv6	-0.0131	-0.0132	-2.67494359995624e-15
fv7	0.0637	0.0638	2.41473507855972e-15
fc1	0.2449	0.245	8.04911692853238e-16
fc2	0.1523	0.1523	-2.99760216648792e-15
fc3	0.1827	0.1827	2.77555756156289e-16
fc4	0.3591	0.3591	5.55111512312578e-17
fc5	0.2669	0.2669	2.22044604925031e-16
fc6	0.1657	0.1658	1.2490009027033e-15
fc7	0.2109	0.2109	-1.47104550762833e-15
fo1	-0.1073	-0.1073	2.63677968348475e-16
fo2	-0.1565	-0.1566	-3.98847621596587e-14
fo3	-0.0686	-0.0686	1.16573417585641e-15
fo4	-0.2521	-0.2522	-6.66133814775094e-16
fo5	0.0045	0.0045	-1.98625837999344e-16
fo6	0.0910	0.0910	-2.63677968348475e-15
fo7	-0.0127	-0.0127	3.85108611666851e-16

**Table A.4.** The fist column represents the symbolic version of the retrieved dynamic friction parameters for the 7R with friction, the second column is the estimated numerical value, the third the real one obtained with the ground-truth parameters while the last column is the identification error. All the 64 coefficients were identified but the first 43 were equal to those identified in the vanilla 7R hence for the ease of reading only the new one were reported here.

Parameter	Loose LB	Loose UB	Normal LB	Normal UB	Tight LB	Tight UB
$m_j$	0	30	0	12	0	6
$c_{1x}$	-0.4	0.4	-0.1	0.1	-0.05	0.05
$c_{1y}$	-0.8	0	-0.4	0	-0.2	0.05
$c_{1z}$	-0.6	0.6	-0.2	0.2	-0.1	0.1
$c_{2x}$	-0.4	0.4	-0.1	0.1	-0.05	0.05
$c_{2y}$	-0.6	0.6	-0.2	0.2	-0.1	0.1
$c_{2z}$	-0.4	0.9	-0.1	0.4	-0.05	0.2
$c_{3x}$	-0.4	0.4	-0.1	0.1	-0.05	0.05
$c_{3y}$	-0.4	0.9	-0.1	0.4	-0.05	0.2
$c_{3z}$	-0.6	0.6	-0.2	0.2	-0.1	0.1
$c_{4x}$	-0.4	0.4	-0.1	0.1	-0.05	0.05
$c_{4y}$	-0.6	0.6	-0.2	0.2	-0.1	0.1
$c_{4z}$	-0.4	0.9	-0.1	0.4	-0.05	0.2
$c_{5x}$	-0.4	0.4	-0.1	0.1	-0.05	0.05
$c_{5y}$	-0.9	0.4	-0.4	0.1	-0.2	0.05
$c_{5z}$	-0.6	0.6	-0.2	0.2	-0.1	0.1
$c_{6x}$	-0.4	0.4	-0.1	0.1	-0.05	0.05
$c_{6y}$	-0.6	0.6	-0.2	0.2	-0.1	0.1
$c_{6z}$	-0.6	0.6	-0.2	0.2	-0.1	0.1
$c_{7x}$	-0.4	0.4	-0.1	0.1	-0.05	0.05
$c_{7y}$	-0.4	0.4	-0.1	0.1	-0.05	0.05
$c_{7z}$	0.4	0.6	0.1	0.2	0.05	0.1
$I_{jxx}, j \neq 6$	0	1	0	0.5	0	0.05
$I_{jxy}, j \neq 6$	-1	1	-0.5	0.5	-0.005	0.005
$I_{jxz}, j \neq 6$	-1	1	-0.5	0.5	-0.005	0.005
$I_{jyy}, j \neq 6$	0	1	0	0.5	0	0.05
$I_{jyz}, j \neq 6$	-1	1	-0.5	0.5	-0.005	0.005
$I_{jzz}, j \neq 6$	0	1	0	0.5	0	0.05
$I_{6xx}$	0	1	0	0.1	0	0.01
$I_{6xy}$	-1	1	-0.2	0.2	-0.002	0.002
$I_{6xz}$	-1	1	-0.2	0.2	-0.002	0.002
$I_{6yy}$	0	1	0	0.1	0	0.01
$I_{6yz}$	-1	1	-0.2	0.2	-0.002	0.002
$I_{6zz}$	0	1	0	0.1	0	0.01
$f_{vj}$	0	100	0	50	0	1
$f_{cj}$	0	100	0	50	0	1
$f_{oj}$	-100	100	-50	50	-1	1

**Table A.5.** Bounds for the 7R with and without friction used in the extraction of dynamic parameters phase. The second and third columns represents the loose bounds over every parameters, the fourth and fifth the normal ones and the sixth and seventh the tight ones. General parameter with index  $j$  means that its bounds are equal among all the joints (or with an exception for a particular joint, e.g.  $j = 6$ ).

Parameter	Loose LB	Loose UB	Normal LB	Normal UB	Tight LB	Tight UB
$m_1$	0	50	0	5	3	4
$m_2$	0	7	0	2	0.5	1
$m_3$	0	12	0	3	0.8	1.5
$c_{1x}$	-0.2	0.2	-0.04	0.04	-0.0005	0.0015
$c_{1y}$	-0.5	0.1	-0.3	0	-0.15	-0.07
$c_{1z}$	-0.2	0.2	-0.04	0.04	0.001	0.003
$c_{2x}$	-0.4	0.1	-0.22	0	-0.1	-0.06
$c_{2y}$	-0.2	0.2	-0.035	0.035	-0.0005	0.0015
$c_{2z}$	-0.2	0.2	-0.035	0.035	0.001	0.003
$c_{3x}$	-0.3	0.1	-0.15	0	-0.08	-0.04
$c_{3y}$	-0.2	0.2	-0.03	0.03	0.001	0.003
$c_{3z}$	-0.2	0.2	-0.03	0.03	0.002	0.004
$I_{jxx}$	0	1	0	0.5	0	0.1
$I_{jxy}$	-1	1	-0.5	0.5	-0.1	0.1
$I_{jxz}$	-1	1	-0.5	0.5	-0.1	0.1
$I_{jyy}$	0	1	0	0.5	0	0.1
$I_{jyz}$	-1	1	-0.5	0.5	-0.1	0.1
$I_{jzz}$	0	1	0	0.5	0	0.1
$f_{vj}$	0	100	0	50	0	1
$f_{cj}$	0	100	0	50	0	1
$f_{oj}$	-100	100	-50	50	-1	1

**Table A.6.** Bounds for the 3R with and without friction used in the extraction of dynamic parameters phase. The second and third columns represents the loose bounds over every parameters, the fourth and fifth the normal ones and the sixth and seventh the tight ones. General parameter with index  $j$  means that its bounds are equal among all the joints.

Set	Setting	Path
p_1	normal bounds    partial loss function	Data/results_sim/normal/3R_1_params.m
p_4	normal bounds    full loss function	Data/results_sim/normal/3R_4_params.m
p_5	tight bounds    partial loss function	Data/results_sim/tight/3R_5_params.m
p_8	tight bounds   full loss function	Data/results_sim/tight/3R_8_params.m
p_9	loose bounds    partial loss function	Data/results_sim/loose/3R_9_params.m
p_12	loose bounds    full loss function	Data/results_sim/loose/3R_12_params.m

**Table A.7.** In the first column there is the id of the set of dynamic parameters, in the second there are the conditions under which it was extracted from the coefficients and in the last column there is the path inside the folder Environment/3R/ in which find the set.

Set	Setting	Path
p_13	normal bounds    partial loss function	Data/results_sim/normal/3R_13_params.m
p_16	normal bounds    full loss function	Data/results_sim/normal/3R_16_params.m
p_17	tight bounds    partial loss function	Data/results_sim/tight/3R_17_params.m
p_20	tight bounds   full loss function	Data/results_sim/tight/3R_20_params.m
p_21	loose bounds    partial loss function	Data/results_sim/loose/3R_21_params.m
p_24	loose bounds    full loss function	Data/results_sim/loose/3R_24_params.m

**Table A.8.** In the first column there is the id of the set of dynamic parameters, in the second there are the conditions under which it was extracted from the coefficients and in the last column there is the path inside the folder `Environment/3R_friction/` in which find the set.

Set	Setting	Path
p_25	normal bounds    partial loss function	Data/results_sim/normal/7R_25_params.m
p_28	normal bounds    full loss function	Data/results_sim/normal/7R_28_params.m
p_29	tight bounds    partial loss function	Data/results_sim/tight/7R_29_params.m
p_32	tight bounds   full loss function	Data/results_sim/tight/7R_32_params.m
p_33	loose bounds    partial loss function	Data/results_sim/loose/7R_33_params.m
p_36	loose bounds    full loss function	Data/results_sim/loose/7R_36_params.m

**Table A.9.** In the first column there is the id of the set of dynamic parameters, in the second there are the conditions under which it was extracted from the coefficients and in the last column there is the path inside the folder `Environment/7R/` in which find the set.

Set	Setting	Path
p_37	normal bounds    partial loss function	Data/results_sim/normal/7R_37_params.m
p_40	normal bounds    full loss function	Data/results_sim/normal/7R_40_params.m
p_41	tight bounds    partial loss function	Data/results_sim/tight/7R_41_params.m
p_44	tight bounds   full loss function	Data/results_sim/tight/7R_44_params.m
p_45	loose bounds    partial loss function	Data/results_sim/loose/7R_45_params.m
p_48	loose bounds    full loss function	Data/results_sim/loose/7R_48_params.m

**Table A.10.** In the first column there is the id of the set of dynamic parameters, in the second there are the conditions under which it was extracted from the coefficients and in the last column there is the path inside the folder `Environment/7R_friction/` in which find the set.

# References

- [1] C. Gaz, M. Cognetti, A. Oliva, P.R. Giordano, A. De Luca. *Dynamic Identification of the Franka Emika Panda Robot With Retrieval of Feasible Parameters Using Penalty-Based Optimization*. IEEE Robotics and Automation Letters, Vol. 4, No. 4, 2019.
- [2] C. Gaz, F. Flacco, A. De Luca. *Extracting Feasible Robot Parameters from Dynamic Coefficients using Nonlinear Optimization Methods*. IEEE International Conference on Robotics and Automation (ICRA), 2016.
- [3] C. D. Sousa, R. Cortesão. *Inertia Tensor Properties in Robot Dynamics Identification: A Linear Matrix Inequality Approach*. IEEE Transaction on Mechatronics, Vol. 24, No. 1, 2019.
- [4] C. Gaz, A. De Luca. *Payload Estimation Based on Identified Coefficients of Robot Dynamics with an Application to Collision Detection*. IEEE/RSJ International Conference on Intelligent Robots and Systems (IROS), 2017.
- [5] C. Gaz, F. Flacco, A. De Luca. *Identifying the Dynamic Model Used by the KUKA LWR: A Reverse Engineering Approach*. IEEE International Conference on Robotics and Automation (ICRA), 2014.